Tug-of-war between cortical and cytoplasmic forces shaping planar of 4-cell stage embryos

Silvia Caballero-Mancebo[1], Daniel Gonzalez Suarez[1], Janet Chenevert[1], Sameh Ben-Aicha[2], Lydia Besnardeau[1], Alex McDougall[1] and Rémi Dumollard[1*]

[1]Laboratoire de Biologie du Développement de Villefranche-sur-Mer, Institut de la Mer de Villefranche-sur-Mer, Sorbonne Université, CNRS, 06230 Villefranche-sur-Mer, France.
[2]Institut de Biologie de Valrose, Université Côte-d'Azur, CNRS, 03108 Nice, France.

* Corresponding author: remi.dumollard@imev-mer.fr

ABSTRACT

Early embryonic cleavages often follow conserved geometric rules, resulting in species-specific cleavage patterns. How these rules are mechanistically implemented, however, varies widely across species and remains poorly understood. Here, using quantitative 3D live imaging, mechanical and biochemical manipulations, we dissect the mechanisms governing centrosomal complex (CC) migration and spindle orientation in ascidian 2-cell stage embryos to generate the characteristic planar, square 4-cell stage. We show that following the first mitotic division, CCs in the two blastomeres form at variable orientations relative to the mother spindle and progressively achieve parallel and coplanar alignment during interphase of the 2-cell stage. Final spindle orientation is established prior to nuclear envelope breakdown, contrasting with dynamic spindle reorientation reported in other systems.

Our analyses reveal that CC rotation is driven by forces acting on long astral microtubules and guided by an anisotropic, ER-rich cytoplasmic domain that surrounds the CCs. This ER domain correlates with a dense astral microtubule network, enabling length-dependent microtubule pulling that orients the CCs independently of cell shape. In parallel, dynein-mediated cortical pulling refines spindle tilt and maintains coplanarity. Together, these findings uncover a cell-cycle-regulated tug-of-war between ER-mediated cytoplasmic forces and anisotropic cortical forces that ensures robust planar cleavage in ascidian early embryos.

INTRODUCTION

Species-specific patterns of early cleavage divisions have fascinated developmental biologists for more than a century. Despite the extraordinary diversity of embryo sizes and shapes, early cleavage planes typically follow two conserved geometric principles: Hertwig's rule, which states that the mitotic spindle aligns along the longest axis of the cell, highlighting the role of cell shape in dictating the orientation of the division plane[1,2] and the Sach's (or orthogonal) rule, where division occurs at right angles to the previous one[3], due to either centrosome chirality or cell shape. These rules collectively explain the widespread emergence of the planar, square arrangement of blastomeres at the 4-cell stage, a configuration observed across a broad spectrum of animal taxa, including cnidarians, echinoderms, ascidians, cephalochordates, and amphibians[4–6]. Yet, despite the apparent universality of these geometric rules, the mechanisms by which they are implemented are species-dependent and remain the subject of active investigation and debate.

In many species, the physical environment of the embryo—such as the presence of a rigid eggshell—can impose significant constraints on blastomere arrangement and cleavage orientation. For example, nematode embryos, encased in a rigid eggshell, display a striking diversity of 4-cell stage morphologies, ranging from square to linear configurations, depending on the mechanical properties and the aspect ratio of the eggshell[7–9]. In contrast, unconfined embryos and embryos with a non-restrictive confinement, such as ascidian and echinoderm embryos, more consistently exhibit the archetypal flat, square 4-cell configuration[10,11]. However, this configuration is far from the mechanically stable configuration of 4 blastomeres – a tetrahedron – but arises due to the short division times of early embryos[8], suggesting that oriented cell divisions underpin the flat and square shape of 4-cell stage embryos.

How spindle positioning is controlled during the first two cell divisions has been studied in many species and the picture so far is clouded by a diversity of behaviors between species of different embryonic size[12–14] and by remaining controversies in the canonical model, the *C. elegans* early embryo, where cytoplasmic pulling and cortical pulling or pushing have all been hypothesized to play a role in spindle orientation[15–18]. To generate a symmetric and flat 4-cell stage embryo, the first two cell divisions must be centered, equal, and at 90° to each other, and the mitotic spindles of each cell of the 2-cell stage embryo must be coplanar and parallel. One modelling approach suggests that geometric constraints coupled to either yolk stratification - as in *Xenopus* or ascidian embryos - or localized cortical factors - as in sea urchin embryos - are sufficient to generate flat 4-cell stage embryos[19]. This theoretical model postulates simply that pulling forces applied to astral microtubules must be proportional to their length[2,20]. Such force proportional to microtubule length is thought to be achieved by dynein-dependent pulling of cytoplasmic cargoes along their whole length. However, the nature of cytoplasmic cargoes remains to be established[19,21].

In smaller cells, cortical pulling forces become more prominent. In culture cells and cells of the *Drosophila* notum epithelium, cortical pulling forces have been shown to be essential in aligning the spindle with the long axis of the cell during interphase[22,23]. In *C. elegans* zygotes/embryos, one model predicts that cortical pulling can mediate alignment to the long axis of the zygote[16], whereas strong cortical pulling has also been shown to align spindles to the short axis of the AB cell in the 2-cell stage embryo before the actomyosin cytokinetic ring refines the alignment along the long axis[17]. A stochiometric theoretical model shows that there are more cortical pulling sites close to the

aster/spindle pole, and the forces generated at these sites result in the off-centering and alignment of the spindle with the short axis of the cell, thus having an opposing action to the length-dependent cytoplasmic pulling forces exerted on astral microtubules[17].

In ascidian embryos, centering cytoplasmic forces and off-centering cortical forces prevail during pronuclei migration in the zygote. Here, cortical pulling forces in the rear end of the sperm aster counteract cytoplasmic pulling forces generated at the front end[24]. In this study, we analyze the centrosome and spindle movements underlying the generation of a flat and square shape in ascidian 4-cell stage embryos. We find that centrosomal complexes (CCs) align progressively with the long length of the blastomeres during interphase when cortical pulling is strong. However, since we find that cortical pulling forces are reduced during mitosis, cortical pulling is likely to be dispensable for the rotation of the centrosomes that may instead rely on cytoplasmic pulling on the ER that is stratified in each cell of the 2-cell stage embryo. In line with this tug-of-war hypothesis, experimentally increasing cortical pulling, and thus interfering with the balance between cortical and cytoplasmic pulling forces, planar 4-cell stage embryos were transformed into non-planar embryos, highlighting that the balance between cytoplasmic and cortical pulling results in a dynamic "tug-of-war" that determines the cleavage pattern in early embryos.

RESULTS

Progressive coplanar and parallel alignment of the two centrosomal complexes at the 2-cell stage

In order to precisely follow the movements of the centrosomal complexes (CCs) during the 2-cell stage, we performed 3D live imaging of embryos injected with EB3-3xVenus to label the CCs from mitosis of 1-cell stage to the beginning of cytokinesis of the 2-cell stage (Fig. 1A, movie 1). In the vegetal view, two distinct centrosomes can be observed at each end of the spindle at anaphase of the 1-cell stage, coinciding with the beginning of cytokinesis of the first mitosis (Fig. 1A- inset, t = 2 min). We found that the CCs in the two forming daughter cells are not initially parallel to each other (in 60% of all analyzed embryos) and progressively align with each other during the interphase of the 2-cell stage, in contrast to *Xenopus* embryos, where the position of the centrosomes following the first mitosis determines the orientation of the spindle and the plane of division at the 2-cell stage[14]. This alignment results in two parallel CCs at nuclear envelope breakdown (NEBD) of the 2-cell stage (Fig. 1A, 16-20 min), which in turn give rise to two parallel spindles at metaphase of the 2-cell stage (Fig. 1A, 20-26 min). To generate the characteristic flat and square geometry of the ascidian 4-cell stage embryo, the two spindles at the 2-cell stage must not only be parallel but also coplanar. A side view (orthogonal to the vegetal view) revealed that, indeed, the two CCs remain largely coplanar throughout the 2-cell stage (Fig. 1A, bottom row).

To further document the complex migration pattern of CCs and how they orient over time, we tracked the position of the anterior and posterior centrosomes within each CC in 3D (Fig. 1B) and measured the rotation and tilt angles of each CC with respect to the mitotic spindle at 1-cell stage (Fig. 1C-D, S1A). We found that initially the CCs form with a rotation of 68.2° ± 24.6 with respect to the mother spindle, and that during interphase of the 2-cell stage, the CCs rotate to form a final angle of 82.5° ± 5.3 with respect to the mitotic spindle at the 1-cell stage by the time the daughter cells are in metaphase of the 2-cell stage. Surprisingly, this final position of the CCs does not change much from

134 the time of NEBD, contrary to what has been observed in other organisms and somatic cells, where
135 the final position of the spindle is fine-tuned during metaphase and anaphase[12,15,22], suggesting that
136 spindle positioning in ascidian embryos is largely predetermined before NEBD rather than dynamically
137 adjusted during mitosis.
138
139 Consistent with this idea, the tilt angle between the CCs and the 1-cell stage spindle also decreased
140 from 25.5° ± 22.4 to 15.1° ± 11.1 (Fig. 1D) but did not converge to zero, as would be expected for a flat
141 square 4-cell stage embryo. This observation is in agreement with previous reports describing a
142 posterior-vegetal tilt of the spindle in ascidians at the 8-cell stage[5]. Comparing the orientation of the
143 sister CCs and spindles at the 2-cell stage further confirmed our observations that they progressively
144 become parallel, as indicated by a reduction in the rotation angle between them from 48.4° ± 25 to
145 6.6° ± 5.5 (Fig. 1E, S1B - Rotation), and coplanar, as reflected by the decrease in the tilt angle between
146 them from 3.9° ± 4.8 to 1.8° ± 3.1 over time (Fig. 1E, S1B - Tilt). Altogether, this analysis revealed that
147 the proper orientation of the CCs required to generate a flat, square 4-cell stage ascidian embryo is
148 progressively established during the end of mitosis at 1-cell stage and interphase at 2-cell stage, and
149 that by the time of mitotic entry at 2-cell stage, the final position of the future spindle is already
150 defined.
151
152 To better understand the mechanisms that orient the CCs during the end of mitosis of the 1-cell stage
153 and interphase of the 2-cell stage, we examined their migration at a higher spatiotemporal resolution
154 (Fig. 2A, movie 2). We found that the CCs form in the center of the daughter cell at some distance from
155 the nucleus (~17 µm) before the first cleavage is complete (Fig. 2A, 30 s, arrowhead), and that the
156 centrosomes within each CC remain close to each other and move together until the end of interphase
157 of the 2-cell stage, when the centrosomes in each CC start to separate from each other and the nucleus
158 positions between them (Fig. 2A-B, 12- 14 min) right before NEBD. Interestingly, the final orientation
159 of CCs is reached when the 2 centrosomes start separating (Fig. 1D-E, 2B) indicating that the rotation
160 of CCs occurs without separation of the centrosomes and suggesting that there is no need for Eg5
161 kinesin activity for CC rotation[25]. Since the centrosomes within a CC remain close together during their
162 migration, we asked whether a physical link between the 2 centrosomes is necessary for their proper
163 migration. To that end, we performed periodic laser ablations every 90 s between the two centrosomes
164 in one of the 2 sister CCs from the time when both centrosomes in each CC were identifiable (anaphase
165 of the 1-cell stage) until the nucleus reached the CC center (Fig. 2C, movie 3). We found that neither
166 rotation nor tilt was affected when centrosomes were ectopically separated by laser ablations (Fig.
167 2C', S2A-B), and that the ablated 2-cell stage embryos still divided into a flat and square 4-cell stage.
168 Because centrosome separation initiates when the nucleus reaches them, we assessed whether the
169 CCs use the nuclei to orient/power their movements as previously observed in *C. elegans* and
170 *Drosophila* embryo[15,26–28]. To test this possibility, we performed periodic laser ablations every 90 s
171 between the CC and the migrating nucleus in one of the two cells from the time both centrosomes in
172 the CC were identifiable until the nuclei reached the center of the CC (Fig. 2D, movie 4). We found that
173 these ablations could impair nucleus migration (Fig. S2C) but did not affect either CC migration or their
174 final orientation (Fig. 2D', S2D), as the CCs/spindles eventually became parallel and coplanar as in
175 control embryos.
176
177 Altogether these results show that CCs movements initiate at anaphase of mitosis I and proceed during
178 cytokinesis and interphase of the 2-cell stage in ascidians. These complex movements do not rely on

179 mechanisms previously described in other embryos such as *Xenopus* embryos[14], or *C. elegans* zygotes[26]
180 or *Drosophila* blastoderm embryos[27,29] and they are not supported by the nuclei or antiparallel
181 microtubules between centrosomes.
182
183 **CCs movements are powered by forces generated by astral microtubules**
184 As the abovementioned mechanisms do not appear to contribute to CC migration, we considered the
185 astral microtubule network as the most likely source of the forces driving CC migration. We first imaged
186 microtubule distribution at key times during CC migration and found that the network of astral
187 microtubules grows at anaphase of mitosis I and expands in the whole volume of the cell during
188 interphase before sharply retracting at prophase of the 2-cell stage (Fig. 3A). To understand how this
189 network remodeling could contribute to the migration of the CCs, we analyzed the density of
190 microtubules from the centrosome to the cell cortex. We found that in interphase (Fig. 3A'), a dense
191 network of microtubules is formed extending from the centrosomes across the central cytoplasm (Fig.
192 3A', blue shaded area), surrounded by a less dense peripheral network of microtubules near the cortex
193 (Fig. 3A', red shaded area). Upon mitotic entry, this organization was lost, and the microtubule network
194 became largely restricted to the pericentrosomal region, with the peripheral population markedly
195 diminished. (Fig. 3A''). The long astral microtubules observed during interphase may be the sites of
196 force generation to move CCs either by cytoplasmic pulling, as demonstrated in sea urchin embryos[2],
197 or by pulling of astral microtubules on the cell cortex previously shown in ascidian zygotes[24]. To test
198 this hypothesis, we performed periodic laser ablations of the astral microtubules (every 90 s) in one of
199 the 2 sister cells (Fig. 3B, movie 5) from the time when both centrosomes in each CC were identifiable
200 (anaphase of the 1-cell stage, 2 min) until NEBD of the 2-cell stage (17 min). We found that rotation of
201 the CCs was severely affected in the ablated cell but not in the non-ablated one (Fig. 3B'), and that the
202 sister CCs/spindles at the 2-cell stage were no longer parallel (Fig. S3A – Rotation Ablated). In contrast,
203 the tilt was not affected by these laser ablations (Fig 3B') and the CCs and spindles remained coplanar
204 (Fig. S3A – Tilt Ablated). To confirm these observations, we interfered with astral microtubules with 2-
205 methoxyestradiol (2ME), known to preferentially affect dynamic microtubules without impairing
206 spindle formation[30]. Incubating zygotes at anaphase of the 1-cell stage with 2ME drastically reduced
207 the size of centrosomal asters during interphase of the 2-cell stage (Fig. 3C) and prevented CC
208 migration, leading to strong defects in both rotation and tilt angles of the spindles at the end of 2-cell
209 stage, losing their coplanarity (Fig. 3C'-D, S3B-C).
210
211 Altogether, these results demonstrate that forces exerted on astral microtubules are responsible for
212 the proper migration and orientation of CCs/spindles in 2-cell stage ascidian embryos. In other
213 systems, such forces are generated by dynein motors through two main mechanisms: cortical pulling
214 forces, produced by dynein motors anchored at the plasma membrane that exert tension on astral
215 microtubules as they move toward their minus ends[22,31–33], and cytoplasmic pulling forces, generated
216 by dynein motors bound to intracellular organelles such as endoplasmic reticulum or endosomes[34–36].
217 To explore the contribution of these mechanisms to the shaping of planar ascidian 4-cell stage
218 embryos, we sought to localize intracellular dynein by immunocytochemistry against the dynein
219 localizing complex dynactin. Using ascidian-specific anti-dynactin antibody (see Materials and
220 Methods, Fig. 3E, S3D), we found that dynactin is enriched both in the pericentrosomal cytoplasm and
221 at the cell cortex. These two pools of dynactin closely correlate with the dense central and the
222 peripheral microtubule populations, respectively, observed in interphase cells (Fig. 3A').
223

224 Together, these findings suggest that dynein–dynactin complexes are enriched on locations supporting
225 a role for both cytoplasmic and cortical pulling in the positioning CCs and spindles. We then sought to
226 discriminate the role of each mechanism in the positioning of the CCs.
227
228 **An anisotropic ER domain may drive CC movements in the ascidian embryo.**
229 We first investigated the cytoplasmic source of force generation. Previous work has shown that the
230 cytoplasm of ascidian embryos is a dense mixture of yolk granules and organelles[37] and that the
231 interaction between cytoskeletal structures and cytoplasmic components generates forces that shape
232 the embryo and drive cytoplasmic organizations[38]. Moreover, recent studies have suggested that
233 astral microtubules are anchored to the endoplasmic reticulum (ER) of the cells via dynein motors and
234 are able to generate pulling and pushing forces, allowing spindles to orient. Because yolk granules in
235 ascidians do not accumulate around the sperm aster, as does the endoplasmic reticulum and, to a
236 lesser extent, the mitochondria of the myoplasm[24], we hypothesize that neither the yolk nor the
237 mitochondria display dynein motors anchored to their surface. We then asked if the ER could serve as
238 the guiding cue for the CCs and spindles to orient. First, we analyzed the distribution of ER over time
239 and found that from mitosis of the 1-cell stage, the spindle and the CCs were surrounded by a cloud of
240 ER (Fig. 4A, S4A, movie 6), closely resembling the pericentrosomal dense astral microtubule population
241 and the localization of dynactin (Fig. 3A, E and S4A). Segmentation and morphometric analysis of the
242 ER associated with the spindle and CCs revealed that, unlike the roughly spherical shape of the cell-
243 averaging 0.85 ± 0.05 sphericity during interphase, the ER forms a cytoplasmic domain with an ellipsoid
244 shape - 0.62 ± 0.04 sphericity - and a clearly defined long axis (Fig. 4B).
245
246 The observed enrichment of microtubules, dynactin, and ER suggests that the ER is covered by dynein
247 motors and thus could be pulled when the ER interacts with astral microtubules. If this were the case,
248 the CCs could leverage this anisotropic ER domain to align with its long axis, as predicted by length-
249 dependent pulling on microtubules to position asters and spindles[39], even in the absence of a
250 geometrically defined long axis of the cell. To address this hypothesis, we quantified the relative
251 alignment between the long axes of the ER domain and the cell, and the CCs/spindles using bootstrap
252 statistics (Fig. 4C). We found that initially, the long axis of the cell, ER, and the CCs are not aligned to
253 each other (Fig. 4C – 2 min, 4D – 2 min), displaying random orientations which results in an average
254 angle of ~45° between the pairs. As cytokinesis and interphase progress, the angle between the long
255 axes of ER and the CCs/spindle gradually decreases, indicating progressive alignment before becoming
256 parallel at the end of interphase (Fig. 4C – 12 min, green; 4D – 12 min, green and grey). In contrast,
257 neither the long axis of the ER domain nor the CCs seem to align with the long axis of the cell over the
258 same period (Fig. 4C), suggesting that cell shape does not provide a dominant cue for spindle
259 orientation. Interestingly, at NEBD, which coincides with the shortening of the astral microtubules, the
260 ER and the forming spindle become momentarily misaligned (Fig. 4C – 17 min, 4D – 17 min), before
261 realigning with the cell axis at the onset of cytokinesis. Together, this analysis shows that the shape of
262 the cell may not provide a consistent geometrical cue for CC orientation, and suggests that, instead,
263 the ER acts as a cytoplasmic scaffold that guides spindle alignment independently of cell geometry,
264 even though the spindles obey the Hertwig rule[39].
265
266 Even though the shape of the 2-cell stage blastomeres remained fairly spherical, there may still be an
267 effect of cell shape in the positioning of the CCs and spindles. To further test whether the ER–spindle
268 alignment depends on external cell geometry or arises intrinsically from cytoplasmic organization, we

269 cultured the embryos in calcium and magnesium-free seawater (CMF) to remove the contribution of
270 cell adhesion (Fig. 4E-G, movie 7). The blastomeres of these embryos were almost perfectly spherical,
271 displaying an average sphericity of 0.96 ± 0.04, and still divided as control ones. The rotation angle
272 between the 2-cell stage CCs relative to the 1-cell spindle, however, was significantly altered, whereas
273 the tilt angle remained unaffected (Fig. 4E'–E''). The delayed rotation of the CCs at the end of the 2-
274 cell stage prevented the mitotic spindles from being parallel at mitosis (Fig. S4B-C), affecting the
275 characteristic square geometry of 4-cell stage embryos and suggesting that cell shape has an
276 instructive role in CC orientation. Nevertheless, the resulting 4-cell stage embryos in CMF remained
277 planar due to the CCs and spindles being coplanar during the whole CC migration (Fig. S4B-C). We then
278 analyzed the shape of the ER domain around CCs and spindles in CMF-cultured embryos, we observed
279 that the ER domain was also less ellipsoidal than in control embryos - average sphericity of 0.91 ± 0.04
280 - supporting the idea that the ER can serve as a proxy for cell shape by reinforcing the cell shape
281 anisotropy. When we compared the alignment dynamics between the ER domain and CCs in CMF
282 embryos, we found that absolute angles were consistently higher than in control embryos, indicating
283 reduced alignment between the ER and the CCs until mitosis of the 2-cell stage when the CCs and ER
284 align together (Fig. 4H). This suggests that cell geometry primarily impacts the progressive alignment
285 of CCs through rotation by cytoplasmic-generated forces, whereas the tilt angle does not seem to be
286 influenced by cell shape.
287
288 **Anisotropic cortical pulling forces maintain the CCs coplanar during CCs migration**
289 Given the established role of cortical pulling forces in spindle orientation across metazoans, and the
290 cortical localization of dynactin we observed (Fig. 3E), we next asked if cortical pulling forces control
291 the observed posterior tilt along the anterior-posterior axis we observe.
292
293 To that end, we first monitored the evolution of cortical pulling forces during CC migration by imaging
294 plasma membrane invaginations after cortical softening with 1 µg/ml Latrunculin B (Fig. 5A-A', movie
295 8)[24,40]. We found that plasma membrane invaginations appear at anaphase of the 1-cell stage and that
296 their frequency increases significantly during interphase of the 2-cell stage before sharply decreasing
297 at prophase and metaphase of the 2-cell stage mitosis (Fig. 5A''). These observations show a good
298 correlation between the appearance of the network of long astral microtubules and the occurrence of
299 cortical pulling, supporting the idea that cortical pulling may also be responsible for CC movements.
300 We then looked at the spatial distribution of cortical pulling sites and found that membrane
301 invaginations were more frequent at the posterior pole of the embryo compared to the anterior pole
302 (Fig. S5A) and that this difference was consistent throughout the migration of the CCs and persisted
303 until anaphase at the 2-cell stage. These findings support our observations of a posterior tilt of the CCs
304 and spindles along the anterior–posterior axis (Fig. 1C, E) and suggest that asymmetrical cortical pulling
305 forces may play a central role in regulating the tilt angle and coplanarity of CCs and spindles, thereby
306 maintaining the planar architecture of the 4-cell stage embryo. Surprisingly, analysis of CCs and spindle
307 orientation in Latrunculin B-treated embryos (Fig. S5B) showed that neither rotation nor tilt angles are
308 affected by drastic softening of the embryo cortex (Fig. S5B') and that the spindles at mitosis of the
309 putative 2-cell stage remain parallel and coplanar (Fig. S5B''). These observations align with previous
310 reports that reducing actomyosin contractility has minimal impact on sperm aster positioning in
311 ascidian zygotes[24] or early spindle orientation[17], and are consistent with studies showing that cortical
312 pulling can persist when actin integrity is compromised[41], while excessive cortical tension can suppress
313 pulling[42]. Thus, the question remains as to whether cortical pulling can regulate CCs movements.

The observation of the posterior bias in cortical pulling forces and its correlation with spindle tilt led us to hypothesize that cortical pulling forces actively control centrosome orientation and that increasing cortical pulling would affect CCs orientation[17] by amplifying spindle tilt which would perturb the coplanarity of the 4-cell stage embryos. In animal cells, cortical pulling forces are mediated by dynein–NuMA–LGN–Gαi complexes anchored to the plasma membrane[22]. In this complex, the heterotrimeric G-protein subunit Gαi recruits LGN to the cortex, which in turn binds NuMA. NuMA then acts as a scaffold linking the cortical complex to astral microtubules, thereby positioning dynein motors to generate pulling forces as they move toward the microtubule minus ends, generating tension from the cortex to astral microtubules and enabling dynein to pull centrosomes and spindles toward specific cortical regions. To test whether increasing cortical pulling alters CCs/spindle positioning and embryo geometry, we overexpressed NuMA and targeted it to the cortex by fusing it to a pleckstrin homology (PH) domain, which promotes membrane localization. In embryos expressing PH-NuMA, the fusion protein predominantly accumulated at the posterior cortex (Fig. 5B, bottom row, 0 min; movie 9). The cortical pulling assay in these embryos confirmed a global increase in the number of plasma membrane invaginations (Fig. 5B', Total) compared to control embryos (Fig. 5A''), with a higher frequency of posterior pulling sites, confirming that cortical pulling was strengthened and correlated with the accumulation of PH-NuMA.

Analysis of the orientation of CCs/spindles in embryos overexpressing cortical NuMA showed a larger tilt angle at the 2-cell stage relative to the spindle at the 1-cell stage, while rotation remained largely unaffected (Fig. 5C-C'', S5D, movie 10). The increased tilt was also reflected in the higher tilt angle between sister spindles at the 2-cell stage (Fig. S5C, S5D - Tilt) that were not coplanar, resulting in embryos adopting a more tetrahedral configuration (Fig. 5C, 26 min), in contrast to the planar geometry observed in controls. Altogether, these results suggest a model in which proper spindle orientation and maintenance of the planar 4-cell embryo geometry depend on a finely tuned tug-of-war between cortical and cytoplasmic dynein-mediated pulling forces acting on astral microtubules in a cell cycle-dependent manner (Fig. 5D).

DISCUSSION

Our study uncovers the mechanisms that drive the dynamic centrosomal complex (CC) migration and spindle orientation in early ascidian embryos and identifies a previously underappreciated balance between cortical and cytoplasmic forces as a key determinant of embryo geometry. Through quantitative live imaging, perturbation assays, and biophysical manipulations, we reveal that ascidian embryos rely on a finely tuned interplay — a tug-of-war — between dynein-dependent forces acting from the cell cortex and those acting from cytoplasmic interactions that are most likely transmitted through the endoplasmic reticulum (ER) network to achieve the characteristic planar 4-cell stage configuration.

Our data provide a comprehensive analysis of the dynamic behavior and mechanisms underlying centrosomal complex (CC) and spindle positioning in 2-cell stage ascidian embryos. We demonstrate that the CCs of the two cells at 2-cell stage initially form at varying angles relative to the position of the first mitotic spindle and progressively achieve parallel alignment during interphase of the 2-cell stage. This progressive alignment is essential for the formation of the characteristic square 4-cell stage

358 ascidian embryo. Interestingly, our study revealed a second cue that drives the coplanarity of the CCs,
359 ensuring the planar arrangement of the blastomeres at 4-cell stage.
360
361 Previous studies in other model organisms have indicated that final spindle orientation is adjusted
362 during mitosis[15,17,22,42]. Notably, our data reveal that in ascidian 2-cell stage embryos, the final
363 orientation of the CCs and the spindle is established before mitotic entry and remains largely
364 unchanged during subsequent mitosis. Our findings reinforce the notion that precise spindle
365 orientation is a critical determinant for embryonic patterning and morphogenesis. The progressive
366 coplanar and parallel alignment of CCs ensures that the resulting 4-cell stage embryo adopts the
367 correct geometry, which is a prerequisite for subsequent morphogenetic events and fate
368 determination in ascidian embryos. Interestingly, the tilt angle between the CCs and the mother
369 spindle does not converge to zero, consistent with previous reports of a posterior-vegetal tilt in
370 ascidian spindles at later stages[5]. Nevertheless, the tilt angle between the CCs/spindles at 2-cell stage
371 is close to zero, essential for the flat, square shape of the 4-cell stage.
372
373 Our results highlight both conserved and divergent mechanisms of spindle orientation across
374 metazoans. In well-studied systems such as *C. elegans*, *Drosophila*, and *Xenopus* embryos, spindle
375 orientation is often dynamically regulated by a combination of cortical pulling forces, nuclear
376 positioning, and microtubule-based mechanisms[26–29]. In these organisms, the mitotic spindle can
377 continue to rotate and adjust its orientation well into mitosis, and dynein-mediated cortical pulling
378 and antiparallel microtubule sliding are critical for proper centrosome positioning[16,17]. In contrast, our
379 laser ablation experiments in ascidian embryos reveal that neither the integrity of the CCs nor the
380 migration of the nucleus is required for the final orientation of the CCs and spindles. Disruption of
381 centrosome separation or nuclear migration does not perturb the progressive alignment of the CCs,
382 nor does it affect the ability of embryos to divide into flat, square 4-cell stage embryos. This finding
383 suggests that ascidian embryos employ a distinct mechanism for spindle orientation that is largely
384 independent of the nuclear or centrosomal cues that are crucial in other systems.
385
386 The discovery that the ER serves as a proxy for cell shape and guides spindle orientation in ascidian
387 embryos has significant implications for the understanding of force generation and spatial organization
388 during early development. It suggests that organelle-based cues can play a dominant role in
389 orchestrating the orientation of cell division by generating cytoplasmic forces that are sufficient to
390 maintain directional coupling, yet whose efficiency depends on geometric constraints imposed by cell–
391 cell contacts. Moreover, the ER-rich domain that forms around the spindle—arising from the local
392 mutual exclusion of both ER sheets and yolk granules—underscores the crucial role that cytoplasmic
393 reorganizations and stratification have in early in development. The spatial organization of the
394 endoplasmic reticulum provides experimental evidence that a stratified cytoplasm can shape where
395 and how intracellular forces are generated and transmitted, which in turn influences spindle
396 behavior[19]. The persistence of planar (but not square) divisions in CMF seawater further implies that
397 cortical inputs primarily refine coplanarity, while ER-based cytoplasmic forces provide the dominant
398 contribution to CC rotation and global spindle alignment.
399
400 Together, these findings support a model in which the positioning of CCs and spindles arises from the
401 integration of two mechanically distinct dynein-driven systems (Fig. 5D). Cytoplasmic pulling forces,
402 transmitted through ER–microtubule coupling, act as a global aligning mechanism that orients the CCs

along a cytoplasmic long axis. In contrast, cortical pulling forces, mediated by the dynein–NuMA complex, provide localized tension that fine-tunes spindle tilt and ensures coplanarity of the embryo. Proper spindle orientation thus depends on a delicate balance: cytoplasmic forces define the overall orientation, whereas cortical forces adjust and stabilize the geometry relative to the embryo's boundaries. Perturbing either component — by weakening microtubule dynamics, increasing cortical pulling, or removing cell shape constraints — disrupts this balance and results in aberrant, non-planar cleavage patterns.

Our findings expand the repertoire of known mechanisms by which cells can achieve precise spatial organization during development and highlight the evolutionary diversity of strategies employed by different organisms. Proper spindle orientation is not only critical for ensuring correct cleavage patterns and cell fate specification but also for the establishment of tissue architecture and organogenesis. The mechanisms uncovered in ascidian embryos may thus inform our understanding of how similar processes are regulated in other organisms, and may provide insights into the evolution of developmental strategies across metazoans.

ACKNOWLEDGEMENTS

We would like to thank Hervé Turlier for fruitful discussions and the Microscopy Imaging Platform (PIM) and the animal facility (CRB) of the Institut de la Mer de Villefranche (IMEV) for their continuous support.

AUTHORS CONTRIBUTIONS

S.C.-M., A.M., and R.D. designed the research. S.C.-M. performed the experiments and analyzed the experimental data. D.G.S. contributed to the data analysis. J.C. performed the immunostainings and antibody validations. S.C.-M. and S.B-A. performed the laser ablation experiments. L.B. created the pSPE3-EB3-mScarlet, pSPE3-Reticulon-Venus, and pSPE3-PH-NuMA-Venus constructs. S.C.-M. and R.D. wrote the manuscript.

FUNDING

The project was funded by the Agence Nationale de la Recherche (France) grant "InvBlastula" (ANR-22-CE13-0036-01)

DATA AVAILABILITY

All relevant data can be found within the article and its supplementary information. All other data supporting the findings of this study are available from the corresponding author on request.

448 **REFERENCES**

449 1. Hertwig, O. *Das Problem der Befruchtung und der Isotropie des Eies: eine Theorie der Vererbung*.
450 (Verlag von Gustav Fischer, 1884).
451 2. Minc, N., Burgess, D. & Chang, F. Influence of Cell Geometry on Division-Plane Positioning. *Cell*
452 144, 414–426 (2011).
453 3. Sachs, J. *Über Die Anordnung Der Zellen in Jüngsten Pflanzentheilen*. (Druck und Verlag der
454 Stahel'schen Buch- & Kunsthandlung, 1877).
455 4. McDougall, A., Chenevert, J., Godard, B. G. & Dumollard, R. Emergence of Embryo Shape During
456 Cleavage Divisions. in *Evo-Devo: Non-model Species in Cell and Developmental Biology* (eds
457 Tworzydlo, W. & Bilinski, S. M.) 127–154 (Springer International Publishing, Cham, 2019).
458 doi:10.1007/978-3-030-23459-1_6.
459 5. Negishi, T., Takada, T., Kawai, N. & Nishida, H. Localized PEM mRNA and Protein Are Involved in
460 Cleavage-Plane Orientation and Unequal Cell Divisions in Ascidians. *Curr. Biol.* 17, 1014–1025
461 (2007).
462 6. Caballero-Mancebo, S. *et al.* Marine Model Organisms for Mechanobiology Studies. *Results Probl.*
463 *Cell Differ.* 76, 91–116 (2026).
464 7. Schulze, J. & Schierenberg, E. Evolution of embryonic development in nematodes. *EvoDevo* 2, 18
465 (2011).
466 8. Giammona, J. & Campàs, O. Physical constraints on early blastomere packings. *PLoS Comput. Biol.*
467 17, e1007994 (2021).
468 9. Krenger, R., Burri, J. T., Lehnert, T., Nelson, B. J. & Gijs, M. A. M. Force microscopy of the
469 Caenorhabditis elegans embryonic eggshell. *Microsyst. Nanoeng.* 6, 29 (2020).
470 10. Minc, N. & Piel, M. Predicting division plane position and orientation. *Trends Cell Biol.* 22, 193–200
471 (2012).
472 11. Grill, S. W. & Hyman, A. A. Spindle Positioning by Cortical Pulling Forces. *Dev. Cell* 8, 461–465
473 (2005).
474 12. Gönczy, P., Grill, S., Stelzer, E. H., Kirkham, M. & Hyman, A. A. Spindle positioning during the
475 asymmetric first cell division of Caenorhabditis elegans embryos. *Novartis Found. Symp.* 237, 164–
476 175; discussion 176-181 (2001).
477 13. Wu, H., Nazockdast, E., Shelley, M. J. & Needleman, D. J. Forces positioning the mitotic spindle:
478 Theories, and now experiments. *BioEssays* 39, 1600212 (2017).
479 14. Wühr, M., Tan, E. S., Parker, S. K., Detrich, H. W. & Mitchison, T. J. A model for cleavage plane
480 determination in early amphibian and fish embryos. *Curr. Biol. CB* 20, 2040–2045 (2010).
481 15. Bondaz, A., Cirillo, L., Meraldi, P. & Gotta, M. Cell polarity–dependent centrosome separation in
482 the C. elegans embryo. *J. Cell Biol.* 218, 4112–4126 (2019).
483 16. Wu, H.-Y. *et al.* Laser ablation and fluid flows reveal the mechanism behind spindle and
484 centrosome positioning. *Nat. Phys.* (2023).
485 17. Middelkoop, T. C. *et al.* A cytokinetic ring-driven cell rotation achieves Hertwig's rule in early
486 development. *Proc. Natl. Acad. Sci.* 121, e2318838121 (2024).
487 18. Kimura, K. & Kimura, A. Intracellular organelles mediate cytoplasmic pulling force for centrosome
488 centration in the Caenorhabditis elegans early embryo. *Proc. Natl. Acad. Sci. U. S. A.* 108, 137–142
489 (2011).
490 19. Pierre, A., Sallé, J., Wühr, M. & Minc, N. Generic Theoretical Models to Predict Division Patterns of
491 Cleaving Embryos. *Dev. Cell* 39, 667–682 (2016).

20. Kimura, K. & Kimura, A. A novel mechanism of microtubule length-dependent force to pull centrosomes toward the cell center. *BioArchitecture* 1, 74–79 (2011).
21. Xie, J. *et al.* Contribution of cytoplasm viscoelastic properties to mitotic spindle positioning. *Proc. Natl. Acad. Sci.* 119, e2115593119 (2022).
22. Anjur-Dietrich, M. I. *et al.* Mechanics of spindle orientation in human mitotic cells is determined by pulling forces on astral microtubules and clustering of cortical dynein. *Dev. Cell* (2024).
23. Unified quantitative characterization of epithelial tissue development | eLife. https://elifesciences.org/articles/08519.
24. Rosfelter, A. *et al.* Reduction of cortical pulling at mitotic entry facilitates aster centration. *J. Cell Sci.* 137, jcs262037 (2024).
25. Yu, W.-X. *et al.* Kinesin-5 Eg5 is essential for spindle assembly, chromosome stability and organogenesis in development. *Cell Death Discov.* 8, 490 (2022).
26. Meyerzon, M. *et al.* Centrosome attachment to the C. elegans male pronucleus is dependent on the surface area of the nuclear envelope. *Dev. Biol.* 327, 433–446 (2009).
27. Buttrick, G. J. *et al.* Akt regulates centrosome migration and spindle orientation in the early Drosophila melanogaster embryo. *J. Cell Biol.* 180, 537–548 (2008).
28. Tanenbaum, M. E. & Medema, R. H. Mechanisms of Centrosome Separation and Bipolar Spindle Assembly. *Dev. Cell* 19, 797–806 (2010).
29. Wong, S.-S., Wainman, A., Saurya, S. & Raff, J. W. Regulation of centrosome size by the cell-cycle oscillator in Drosophila embryos. *EMBO J.* 43, 414–436 (2024).
30. Kamath, K. *et al.* 2-Methoxyestradiol suppresses microtubule dynamics and arrests mitosis without depolymerizing microtubules. *Mol. Cancer Ther.* 5, 2225–2233 (2006).
31. Laan, L. *et al.* Cortical Dynein Controls Microtubule Dynamics to Generate Pulling Forces that Reliably Position Microtubule Asters. *Cell* 148, 502–514 (2012).
32. Kiyomitsu, T. The cortical force-generating machinery: how cortical spindle-pulling forces are generated. *Curr. Opin. Cell Biol.* 60, 1–8 (2019).
33. Omer, S., Greenberg, S. R. & Lee, W.-L. Cortical dynein pulling mechanism is regulated by differentially targeted attachment molecule Num1. *eLife* 7, e36745 (2018).
34. Stefano, G., Renna, L. & Brandizzi, F. The endoplasmic reticulum exerts control over organelle streaming during cell expansion. *J. Cell Sci.* 127, 947–953 (2014).
35. Woźniak, M. J. *et al.* Role of kinesin-1 and cytoplasmic dynein in endoplasmic reticulum movement in VERO cells. *J. Cell Sci.* 122, 1979–1989 (2009).
36. Shamipour, S., Caballero-Mancebo, S. & Heisenberg, C.-P. Cytoplasm's Got Moves. *Dev. Cell* 56, 213–226 (2021).
37. Stoev, I. D. *et al.* Active and Probe-Free Intracellular Rheology via Phase-Sensitive Thermoviscous Flows. 2025.04.07.647540 Preprint at https://doi.org/10.1101/2025.04.07.647540 (2025).
38. Caballero-Mancebo, S. *et al.* Friction forces determine cytoplasmic reorganization and shape changes of ascidian oocytes upon fertilization. *Nat. Phys.* 20, 310–321 (2024).
39. Dumollard, R. *et al.* The invariant cleavage pattern displayed by ascidian embryos depends on spindle positioning along the cell's longest axis in the apical plane and relies on asynchronous cell divisions. *eLife* 6, e19290 (2017).
40. Godard, B. G., Dumollard, R., Heisenberg, C.-P. & McDougall, A. Combined effect of cell geometry and polarity domains determines the orientation of unequal division. *eLife* 10, e75639 (2021).
41. Redemann, S. *et al.* Membrane Invaginations Reveal Cortical Sites that Pull on Mitotic Spindles in One-Cell C. elegans Embryos. *PLOS ONE* 5, e12301 (2010).

537 42. Kelkar, M. *et al.* Spindle reorientation in response to mechanical stress is an emergent property of
538 the spindle positioning mechanisms. *Proc. Natl. Acad. Sci.* 119, e2121868119 (2022).
539
540
541 **MATERIALS AND METHODS**
542 *Biological material*
543 Adult *Phallusia mammillata* were collected in Sète (France) and kept at 16 °C in the aquaria of the
544 Centre de Resources Biologiques (CRB) of the Institut de la Mer de Villefranche (IMEV) which is an
545 EMBRC-France certified service (https://www.embrc-france.fr/fr/nos-services/fourniture-de-
546 ressources-biologiques/organismes-modeles/ascidie-phallusia-mammillata). All experiments
547 were performed at 18-19 °C. Oocytes and sperm were obtained after animal dissection and were
548 used on the day of collection. Oocytes were chemically dechorionated in a 0.1 % trypsin solution
549 (Sigma-Aldrich, T8003) in micro-filtered natural sea water (MFSW; Nalgene 0.2 µm filters, cat. no.
550 Z370584) for 90 min under gentle stirring and kept in until fertilization with 6 µl sperm that was
551 activated by resuspension in 1 ml of MSFW at pH 9.2.
552 Embryos were cultured either in MFSW or in Ca2+ and Mg2+-free sea water (CMF) supplemented
553 with 1 mM EDTA[43].
554
555 *Cloning of expression constructs*
556 To generate the pSPE3-EB3-mScarlet plasmid, the EB3 coding sequence was amplified from pRN3-
557 EB3-3xVenus vector using the following primers with EcoRI and XhoI sites, respectively: 5'-
558 GAATTCAAAATGGCCGTCAATGTGTACTCCACAT-3' and 5'-
559 CTCGAGGTACTCGTCCTGGTCTTCTTGTTGA-3'. The mScarlet coding sequence (including stop
560 codon) was amplified from the plasmid pSPE3-iMyo-mScarlet[38] using the following primers with
561 XhoI and NotI sites, respectively: 5'-CTCGAGATGGTGAGCAAGGGCGAGGCAGTG-3' and 5'-
562 GCGGCCGCCTACTTGTACAGCTCGTCCATGCC-3'. To generate the pSPE3-EB3-mScarlet plasmid, the
563 PCR products were ligated into a pSPE3-Rfa destination vector that had been previously digested
564 with EcoRI and NotI.
565 To generate the pSPE3-Reticulon-Venus plasmid, the reticulon coding sequence was amplified
566 using the following primers: 5'-CACCATGGAGTATGAAACGAGCCC-3' and 5'-
567 CTCTGCTTTAGGCTTGGCACC-3'. The PCR product was used to generate an entry vector using the
568 pDONR/TOPO (p3M-Reticulon). The entry vector was recombined with the destination vector
569 pSPE3-Rfa-Venus.
570 To generate the pSPE3-PH-NuMA-Venus plasmid, the PH and NuMA coding sequences were
571 amplified using hybridizing primers as follows: 5'-AAGCAGGCTCCGCGGCCGCCCCCTTCA-3' and 5'-
572 GAGCTCAACATCATGGATGATGACGAAA-3' for PH and 5'-GAGCTCAACATCATGGATGATGACGAAA-
573 3' and 5'-GTCTGAATCCAAAAAAGAAGGGTGGGCG-3' for NuMA. After hybridization, the full PH-
574 NuMA coding sequence was amplified using the following primers: 5'-
575 ACAAGTTTGTACAAAAAAGCAGGCTCCGCGGCCGCCCCCTTCA-3' and 5'-
576 GTCTGAATCCAAAAAAGAAGGGTGGGCGCGCCGACCCAGCTTTCTTGTACAAAGTGGT-3'. The final
577 PCR product was used to generate an entry vector using the pDONR/TOPO (p3M-PH-NuMA). The
578 entry vector was recombined with the destination vector pSPE3-Rfa-Venus[44].
579

580 *mRNA microinjections*
581 Microinjections were performed as described[45]. Microinjection needles (Harvard Apparatus, 30-
582 0035) were pulled with a PN-30 puller (Narishige) and mounted on a micromanipulation setup
583 (MMO-203, Narishige) attached to an Olympus IX70 microscope. Dechorionated unfertilized eggs
584 were placed into a glass wedge mounted onto a 400 µl Perspex mounting chamber (see for
585 detailed protocol McDougall et al., 2014). *In vitro* mRNA synthesis was performed using the
586 mMESSAGE mMACHINE T3 Transcription Kit 562 (Ambion, AM1343). The following mRNAs were
587 injected: EB3-Venus[24], EB3-mScarlet (this study), Ensconsin-3xGFP[46], Ensconsin-dTomato[46], H2B-
588 Venus[47], PH-dTomato[47], PH-NuMA-Venus (this study), and Reticulon-Venus (this study). mRNAs
589 were injected at a concentration of 2-4 µg/µl using a high-pressure system (Narishige IM300) and
590 incubated at 16 °C overnight before the experiment.
591
592 *Myoplasm and plasma membrane labeling*
593 Dechorionated unfertilized oocytes or zygotes were incubated in a 1 µM solution of MitoTracker™
594 Deep Red FM (Thermo Fisher, M22426) to label the myoplasm and/or in a 1 µM solution of
595 CellMask™ Orange (Thermo Fisher, C10045) in MFSW for 5 min and washed in MFSW before
596 imaging.
597
598 *Cytoskeletal inhibitors*
599 To soften the cortex, 1 µg/ml Latrunculin B (Sigma-Aldrich, L5288) was added to the imaging dish 40
600 minutes post fertilization (right before first cell division) and left in the medium for the remainder of
601 the experiment.
602 To interfere with dynamic microtubules, 1 µg/ml 2-methoxyestradiol (Merck, 362-07-2) was added to
603 the imaging dish 40 minutes post fertilization (right before first cell division) and left in the medium for
604 the remainder of the experiment.
605
606 *Confocal live imaging*
607 Embryos were mounted 40 minutes post fertilization in glass bottom dishes (Cellvis, D35-10-0-N)
608 coated with 1% low melting point agarose (Thermo Fisher, 16500100) in MFSW. Embryos were imaged
609 in either an inverted Leica TCS SP8 confocal microscope or an inverted Leica Stellaris confocal
610 microscope using a HCPL APO CS2 40x/1.1 NA water immersion objective (Leica) and Hybrid detectors.
611 Embryos were imaged *in toto* with an optical section thickness of 3 µm every 120-180 s. For membrane
612 invagination experiments, the frame rate was reduced to 30 s and for fixed samples, the optical section
613 was 1 µm.
614
615 *Laser ablation*
616 Embryos were mounted 40 minutes post fertilization as for confocal live imaging and imaged on a Zeiss
617 LSM980 confocal microscope equipped with a two-photon pulsed laser using a C-Aprochromat 40x/1.1
618 NA water immersion objective. Microtubules between centrosomes or between centrosomes and the
619 nucleus were cut along a 10 µm line and astral microtubules were cut along 50 µm lines in 3 z planes,
620 all of which were performed with a two-photon Coheren Axon 920-2 laser (2.5W). For ablation, the
621 two-photon laser was used at full power, and the power received at the focal point is estimated at 2.8
622 $\cdot 10^{12}$ W/m^2. Embryos were imaged over 50 central z-slices with an optical section thickness of 1 µm
623 every 13 s.

624 *Antibody production*
625 The anti-dynactin mouse polyclonal antibody was produced by fusing 1002 base pairs, amino acids 35
626 to 334, of the *Ciona intestinalis* dynactin subunit 1 protein (GenBank AP042712.1) to a 6-His tag at the
627 C terminus and cloned into the vector pET11. Expression in bacteria was induced with IPTG, and the
628 dynactin fusion protein was purified on a nickel column and eluted with imidazole according to the
629 manufacturer (Potrino Ni-NTA column, Macherey-Nagel). Immunization of mice was performed by
630 Covalab (France), and sera obtained after 57 days were used directly without further purification.
631
632 *Immunostaining*
633 Embryos were fixed in 100% methanol (VWR Chemicals, 67-56-1), which had been pre-chilled at −20°C,
634 and then stored at -20°C. Samples were rehydrated by three washes in PBS containing 0.1% Tween
635 (PBS-Tw), then blocked in PBS-Tw containing 1% BSA for 1 hour at room temperature. Primary
636 antibodies to tyrosinated alpha tubulin (rat anti-alpha-tubulin tyrosinated, monoclonal YL1/2, Merck,
637 MAB1864-I) or to dynactin subunit 1 (mouse polyclonal, custom made, see above) were added at a
638 dilution of 1/500 in blocking buffer and incubated for at least 24 hours at 4 °C. After incubation,
639 samples were washed three times in PBS-Tw, and fluorescent anti-rat (Jackson ImmunoResearch) or
640 anti-mouse secondary antibodies (Jackson ImmunoResearch) were added at a dilution of 1/200. After
641 further incubation at room temperature for 1-2 hours, samples were washed in PBS-Tw, labelled with
642 Hoechst 33342 (final concentration 5 µg/ml, Thermo Fisher, 23491-52-3) for 10 minutes, washed twice
643 more in PBS-Tw, and mounted on glass slides in CitiFluor AF1 (Electron Microscopy Services, 17970-
644 25). To prevent embryo compression or breakage, coverslips were elevated by application of small
645 spacers of modelling clay at the corners as described (ref).
646
647 *Western blot*
648 Anti-dynactin antibody's specificity was validated by Western blot analysis showing a single band at
649 ~55 kDa corresponding to dynactin (Fig. S3D).
650 2 and 8-cell stage embryos were collected in a small volume of MFSW and mixed with the same volume
651 of 2x Laemmli sample buffer (100 mM Tris-HCL pH 6.8, 4% SDS, 0.2% Bromophenol Blue, 20% glycerol
652 and 200 mM dithiothreitol). Samples were heated for 5 min at 95 °C and then stored at -20 °C. Proteins
653 were separated by electrophoresis on SDS-polyacrylamide gels and transferred to a nitrocellulose
654 membrane. Membranes were stained briefly with Ponceau-S, then washed with TBS-Tw (20 mM Tris
655 Base and 150 mM NaCl plus 0.1% Tween-20), and blocked for at least 1 hour in TBS-Tw containing 5%
656 dry milk powder. Immunoblots were then incubated in anti-dynactin primary antibody diluted 1:1000
657 overnight at 4 °C. Membranes were then washed three times with TBS-Tw and incubated with an anti-
658 mouse horseradish peroxidase-conjugated secondary antibody (Jackson ImmunoResearch, 115-035-
659 003) at 1:10,000 dilution in TBS-Tw + 5% dry milk powder for 2 hours at room temperature. After three
660 washes in TBS-Tw, signal detection was carried out using the SuperSignal™ West PLUS Pico
661 chemiluminescent substrate (ThermoFisher Scientific, 34580) and images were acquired with a Fusion
662 FX system (Vilber Lourmat, Collegien, France).
663
664 *3D tracking of centrosomes and angle quantification*
665 Confocal fluorescent Z-stacks of embryos injected with EB3-3xVenus and PH-dTomato were stabilized
666 using the MultiStackReg[48] plugin in Fiji[49]. Centrosomes were then tracked using the MTrackJ[50] plugin
667 in Fiji, and their 3D coordinates (Ci_x, Ci_y, Ci_z) were used to calculate the polar angles (rotation and
668 tilt) with the y-axis (embryonic anterior-posterior axis) as reference.

669 *Centrosome separation*
670 The 3D coordinates of each centrosome were used to calculate the distance between each centrosome
671 within a CC: d = $\sqrt{(C1_x - C2_x)^2 + \left(C1_y - C2_y\right)^2 + (C1_z - C2_z)^2}$
672
673 *Distance between nucleus and CC*
674 Confocal fluorescent Z-stacks of embryos injected with H2B-Venus and EB3-mScarlet were stabilized
675 using MultiStackReg plugin in Fiji. Centrosomes were then tracked using the MTrackJ plugin in Fiji and
676 their 3D coordinates (Ci_x, Ci_y, Ci_z) used to calculate the midpoint of the CC, $M_{CC} =$
677 $\left(\frac{C1_x+C2_x}{2}, \frac{C1_y+C2_y}{2}, \frac{C1_z+C2_z}{2}\right)$. The nucleus of each cell was segmented and tracked using the Surface
678 tool in Imaris (Bitplane). Then the distance at every time point between the nucleus (Ni_x, Ni_y, Ni_z)
679 and the CC midpoint was calculated: $d = \sqrt{(M_x - N_x)^2 + \left(M_y - N_y\right)^2 + (M_z - N_z)^2}$. The radius
680 of the nucleus was subtracted from the distance to reflect the time when the edge of the nucleus
681 reaches the center of the CC.
682
683 *Microtubules intensity profile*
684 The intensity profiles of microtubules were made using the line tool of 15-pixel thickness in Fiji from
685 the centrosome to the plasma membrane. The intensity values shown were normalized to the
686 maximum intensity value along each line. The distance between the centrosome and the plasma
687 membrane was also normalized.
688
689 *Membrane invagination quantification*
690 Confocal fluorescent Z-stacks of embryos incubated in CellMask™ Orange to label the plasma
691 membrane were stabilized using MultiStackReg plugin in Fiji. 10 confocal z-slides over the equator of
692 the embryo were sum projected. The number of membrane invaginations was counted manually by
693 counting the invaginations present at 2-10 µm from the plasma membrane[24] at the times indicated in
694 Fig. 5A' and B.
695
696 *Endoplasmic Reticulum segmentation*
697 Confocal fluorescent Z-stacks of embryos injected with either Reticulon-Venus and PH-dTomato,
698 Reticulon-Venus and Ensconsin-dTomato or Reticulon-Venus and EB3-mScarlet were stabilized using
699 the MultiStackReg plugin in Fiji. For segmentation a Gaussian filter (sigma = 2) was applied and
700 segmented using Ilastik software[51] and the pixel classification method.
701
702 *Plasma membrane segmentation*
703 Confocal fluorescent Z-stacks of embryos injected with PH-dTomato were stabilized using the
704 MultiStackReg plugin in Fiji and segmented using Cellpose[52].
705
706 *Shape analysis*
707 Principal component analysis (PCA) of segmented membrane and ER timelapses was performed in
708 order to obtain the direction of the 3 main axes using a custom-made Python script. To compute the
709 length of the main axes (a, b, c), each voxel from the segmented images was projected onto each axis,
710 and sphericity was calculated as: $sphericity = \sqrt[3]{c^2/ab}$.
711

Data analysis and statistics

Statistical analysis was performed using Prism 8 (GraphPad). The statistical test used in each case and the resulting P values are indicated in each figure legend. N was considered an independent experiment, and n denotes the number of cells; N and n are indicated in each figure. No statistical method was used to predetermine sample size. The experiments were not randomized.

METHODS-SPECIFIC REFERENCES

43. Sardet, C. *et al.* Embryological Methods in Ascidians: The Villefranche-sur-Mer Protocols. in *Vertebrate Embryogenesis: Embryological, Cellular, and Genetic Methods* (ed. Pelegri, F. J.) 365–400 (Humana Press, Totowa, NJ, 2011). doi:10.1007/978-1-61779-210-6_14.
44. Roure, A. *et al.* A Multicassette Gateway Vector Set for High Throughput and Comparative Analyses in Ciona and Vertebrate Embryos. *PLOS ONE* 2, e916 (2007).
45. McDougall, A., Lee, K. W.-M. & Dumollard, R. Microinjection and 4D fluorescence imaging in the eggs and embryos of the ascidian Phallusia mammillata. *Methods Mol. Biol. Clifton NJ* 1128, 175–185 (2014).
46. Costache, V. *et al.* Kif2 localizes to a subdomain of cortical endoplasmic reticulum that drives asymmetric spindle position. *Nat. Commun.* 8, 917 (2017).
47. Prodon, F. *et al.* Dual mechanism controls asymmetric spindle position in ascidian germ cell precursors. *Development* 137, 2011–2021 (2010).
48. Thevenaz, P., Ruttimann, U. E. & Unser, M. A pyramid approach to subpixel registration based on intensity. *IEEE Trans. Image Process.* 7, 27–41 (1998).
49. Schindelin, J. *et al.* Fiji: an open-source platform for biological-image analysis. *Nat. Methods* 9, 676–682 (2012).
50. Meijering, E., Dzyubachyk, O. & Smal, I. Methods for Cell and Particle Tracking. in *Methods in Enzymology* vol. 504 183–200 (Elsevier, 2012).
51. Berg, S. *et al.* ilastik: interactive machine learning for (bio)image analysis. *Nat. Methods* 16, 1226–1232 (2019).
52. Stringer, C., Wang, T., Michaelos, M. & Pachitariu, M. Cellpose: a generalist algorithm for cellular segmentation. *Nat. Methods* 18, 100–106 (2021).

FIGURES

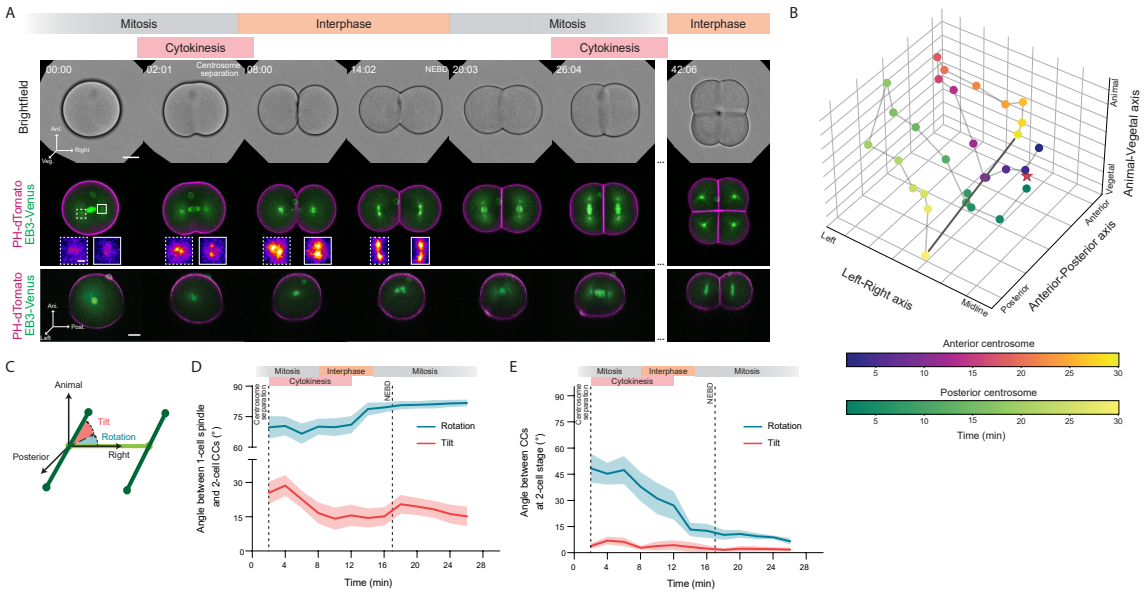

Figure 1: The two CCs become parallel and coplanar during interphase of the 2-cell stage.

(A) Brightfield, confocal fluorescent images of a central z-slide of the plasma membrane (magenta), and maximum intensity projections of centrosomes (green) in a representative ascidian embryo from 1-cell stage metaphase (time = 00:00) to 4-cell stage interphase (time = 40:05). The top and middle rows show the vegetal view, and the bottom row shows the side view. Insets are high magnifications of the left (dashed square) and right (solid square) CCs. Ant. is anterior, Veg. is vegetal, Ani. is animal, Post. is posterior, and NEBD is nuclear envelope breakdown. Time is in minutes:seconds. Scale bar, 30 µm. Inset scale bar, 5 µm.

(B) Example of a 3D plot of the relative positions over time of the anterior and posterior centrosomes of the CC in the left cell of a 2-cell stage ascidian embryo. Time is coded in the respective color bar for each centrosome. The star represents the position of the left centrosome of the mitotic spindle at 1-cell stage, and the grey line represents the final orientation of the spindle at mitosis of the 2-cell stage.

(C) Graphical representation of the tilt and rotation angles between the CCs and the spindles at the 2-cell stage (dark green) and the spindle at the 1-cell stage (light green). Embryonic axes are shown for reference.

(D) Plot of the rotation (blue) and tilt (red) angles between the CCs and the spindle at 2-cell stage and the spindle at 1-cell stage as a function of time after centrosome separation (2 min, dashed vertical line). The dashed line at 17 min indicates the time of NEBD. *N* = 9 embryos, *n* = 18 cells. Error bars, standard error of the mean (s.e.m.).

(E) Plot of the rotation (blue) and tilt (red) angles between the left and right CCs and spindles at 2-cell stage as a function of time after centrosome separation (2 min, dashed vertical line). The dashed line at 17 min indicates the time of NEBD. *N* = 9 embryos. Error bars, standard error of the mean (s.e.m.).

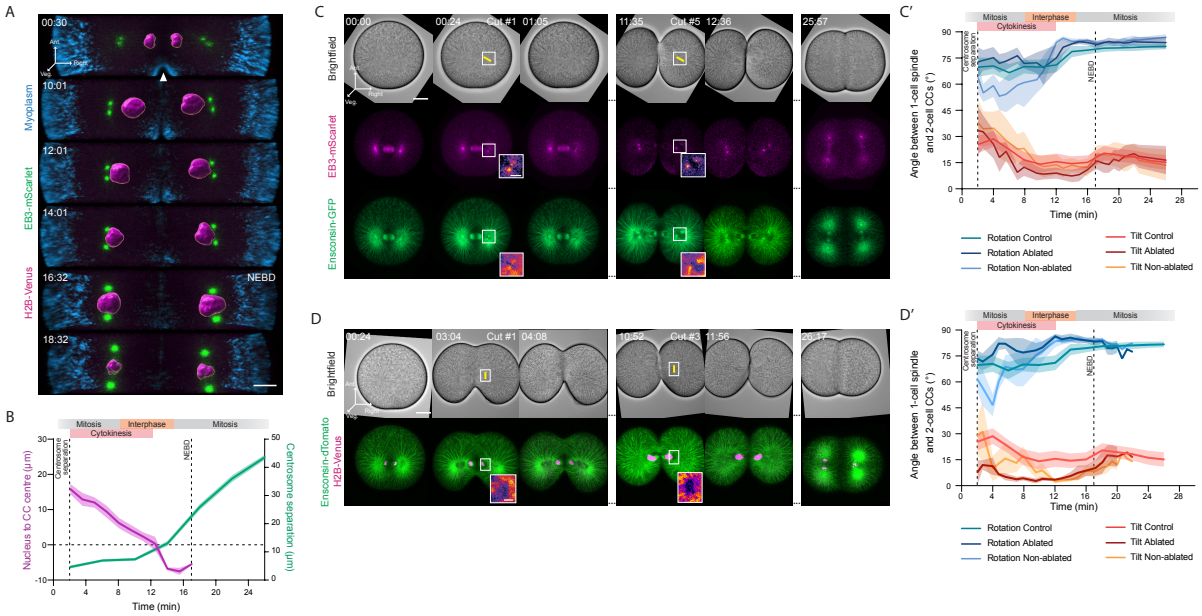

Figure 2: Migration of the CCs and nucleus during interphase of the 2-cell stage.

(A) Confocal maximum intensity projections of the centrosomes (green), mitochondria (cyan), and segmented nuclei (magenta) in a representative ascidian embryo during interphase of the 2-cell stage. Ant. is anterior, Veg. is vegetal, and NEBD is nuclear envelope breakdown. Arrowhead demarcates the ingressing cytokinetic furrow. Time is in minutes:seconds. Scale bar, 10 µm

(B) Plot of the distance between the edge of the nucleus and the center of the CC (magenta, left *y* axis; *N* = 6 embryos, *n* = 12 cells) and the separation of the centrosomes within a CC (green, right *y* axis; *N* = 9 embryos, *n* = 18 cells) as a function of time after centrosome separation (2 min, dashed vertical line). The dashed line at 17 min indicates the time of NEBD. Error bars, standard error of the mean (s.e.m.).

(C) Brightfield and maximum intensity projections of confocal fluorescent images of centrosomes (magenta, middle row) and microtubules (green, bottom row) during laser ablation of microtubules between the centrosomes. The yellow line demarcates the ablation site. The square demarcates the area of the inset. Ant. is anterior, Veg. is vegetal. Time is in minutes:seconds. Scale bar, 30 µm. Inset scale bar, 5 µm.

(C') Plot of the rotation and tilt angles between the CCs and the spindle at 2-cell stage and the spindle at 1-cell stage as a function of time after centrosome separation (2 min, dashed vertical line) in control embryos (*N* = 9 embryos, *n* = 18 cells), ablated cell (*N* = 5 embryos, *n* = 5 cells), and non-ablated cell (*N* = 5 embryos, *n* = 5 cells) in laser-ablated embryos between the centrosomes. The dashed line at 17 min indicates the time of NEBD. Error bars, standard error of the mean (s.e.m.).

(D) Brightfield and maximum intensity projections of confocal fluorescent images of the DNA (magenta) and microtubules (green) during laser ablation of microtubules between the nucleus and the CC. The yellow line demarcates the ablation site. The square demarcates the area of the inset. Ant. is anterior, Veg. is vegetal. Time is in minutes:seconds. Scale bar, 30 µm. Inset scale bar, 5 µm.

(D') Plot of the rotation and tilt angles between the CCs and the spindle at 2-cell stage and the spindle at 1-cell stage as a function of time after centrosome separation (2 min, dashed vertical line) in control embryos (*N* = 9 embryos, *n* = 18 cells), ablated cell (*N* = 4 embryos, *n* = 4 cells), and non-ablated cell (*N* = 4 embryos, *n* = 4 cells) in laser-ablated embryos between the centrosomes and the nucleus. The dashed line at 17 min indicates the time of NEBD. Error bars, standard error of the mean (s.e.m.).

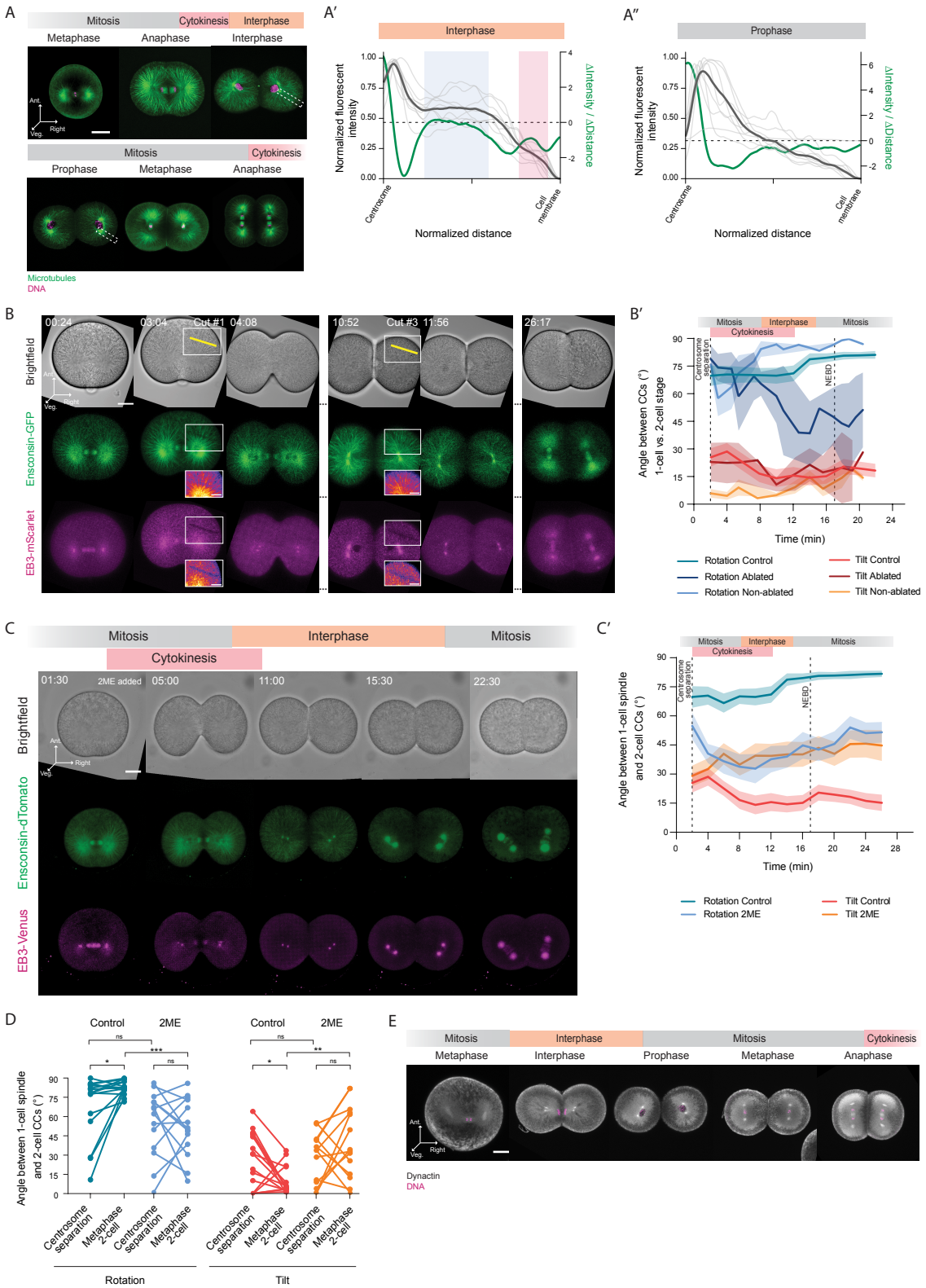

Figure 3: Forces generated along astral microtubules are essential for the orientation of CCs.
(A) Confocal images of a central z-slice of ascidian embryos from 1-cell stage metaphase to 2-cell stage anaphase stained for microtubules (green) and DNA (magenta). Ant. is anterior, Veg. is vegetal. The dashed area indicates the analyzed area in A' and A''. Scale bar, 40 µm.

820 **(A’, A’’)** Fluorescent intensity profiles show the distribution of microtubules from the centrosome to
821 the cell membrane in embryos in interphase (left *y* axis; *N* = 9 embryos) and in prophase (left *y* axis; *N*
822 = 8 embryos). The green line (right *y* axis) represents the change in the average intensity profile over
823 the distance.
824 **(B)** Brightfield and maximum intensity projections of confocal fluorescent images of microtubules
825 (green, middle row) and centrosomes (magenta, bottom row) during laser ablation of astral
826 microtubules. The yellow line demarcates the ablation site. The square demarcates the area of the
827 inset. Ant. is anterior, Veg. is vegetal. Time is in minutes:seconds. Scale bar, 30 µm. Inset scale bar, 20
828 µm.
829 **(B’)** Plot of the rotation and tilt angles between the CCs and the spindle at 2-cell stage and the spindle
830 at 1-cell stage as a function of time after centrosome separation (2 min, dashed vertical line) in control
831 embryos (*N* = 9 embryos, *n* = 18 cells), ablated cell (*N* = 4 embryos, *n* = 4 cells), and non-ablated cell (*N*
832 = 4 embryos, *n* = 4 cells) in laser-ablated embryos. The dashed line at 17 min indicates the time of
833 NEBD. Error bars, standard error of the mean (s.e.m.).
834 **(C)** Brightfield and maximum intensity projections of confocal fluorescent images of microtubules
835 (green, middle row) and centrosomes (magenta, bottom row) in embryos treated with 1µg/ml 2-
836 methoxyestradiol (2ME). Ant. is anterior, Veg. is vegetal. Time is in minutes:seconds. Scale bar, 30 µm.
837 **(C’)** Plot of the rotation and tilt angles between the CCs and the spindle at 2-cell stage and the spindle
838 at 1-cell stage as a function of time after centrosome separation (2 min, dashed vertical line) in control
839 embryos (*N* = 9 embryos, *n* = 18 cells) and embryos treated with 2ME (*N* = 7 embryos, *n* = 14 cells). The
840 dashed line at 17 min indicates the time of NEBD. Error bars, standard error of the mean (s.e.m.).
841 **(D)** Plot of the initial (Centrosome separation) and final (Metaphase 2-cell) rotation (left) and tilt (right)
842 angles between the CCs and the spindle at 2-cell stage with respect to the spindle at 1-cell stage in
843 control embryos (*N* = 9 embryos, *n* = 18 cells; rotation: paired Wilcoxon test, *P=0.0131; tilt: paired
844 Wilcoxon test, *P=0.0250) and embryos treated with 2-methoxyestradiol (*N* = 7 embryos, *n* = 14 cells;
845 rotation and tilt: paired t test, ns - not significant). Control vs. 2ME rotation angle: Kruskal-Wallis test
846 (***P=0.0001) with Dunn's multiple comparisons test (ns – not significant, ***P=0.0001). Control vs.
847 2ME tilt angle: Kruskal-Wallis test (*P=0.0101) with Dunn's multiple comparisons test (ns – not
848 significant, **P<0.0025).
849 **(E)** Confocal images of a central z-slice of ascidian embryos from 1-cell stage metaphase to 2-cell stage
850 anaphase stained for dynactin (grey) and DNA (magenta). Ant. is anterior, Veg. is vegetal. Scale bar, 30
851 µm.
852
853
854
855
856
857
858
859
860
861

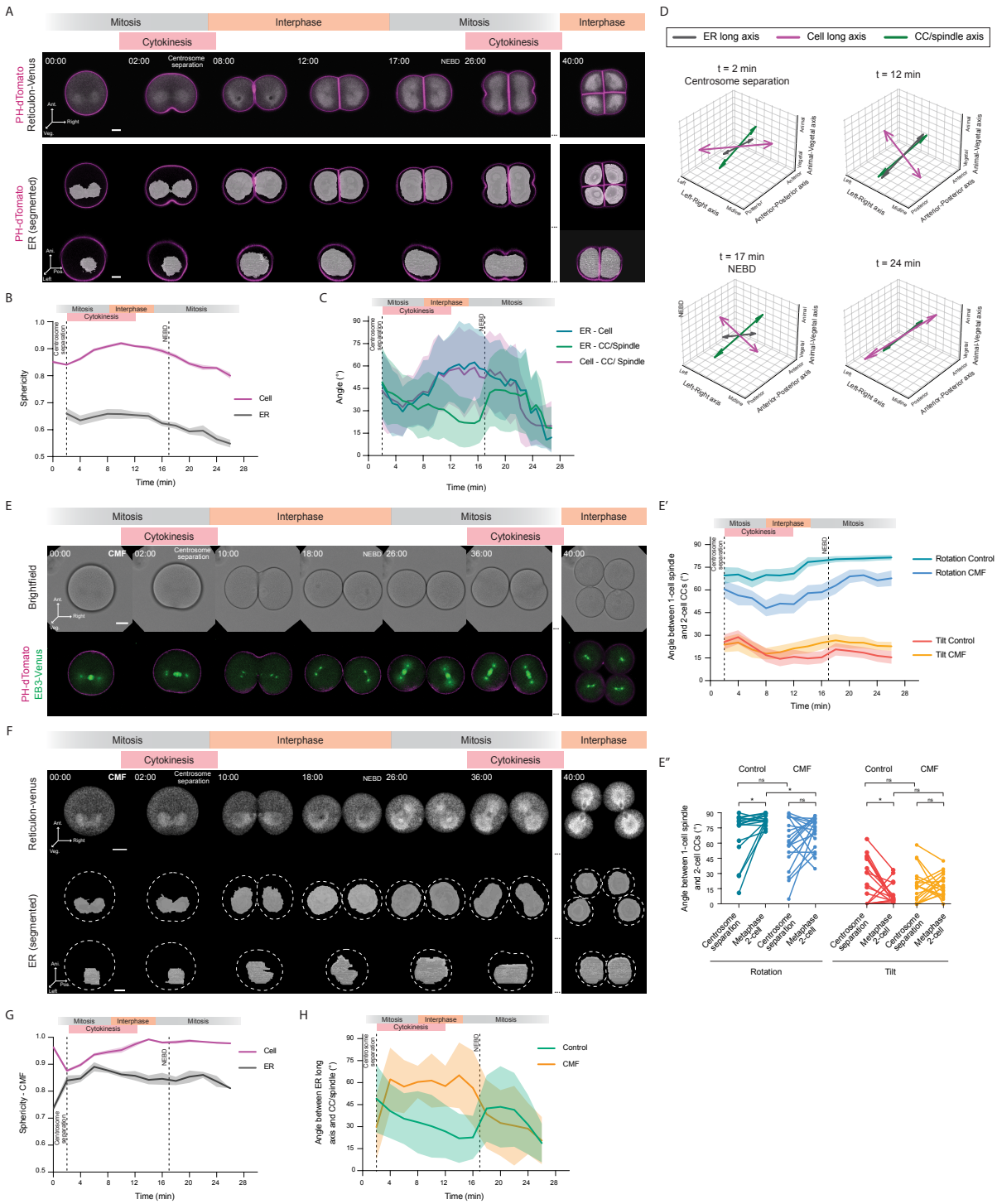

Figure 4: Cytoplasmic pulling controls the rotation of the CCs.

(A) Confocal fluorescent images of a central z-slice of the plasma membrane (magenta) and the endoplasmic reticulum (grey) in a representative ascidian embryo from 1-cell stage metaphase to 4-cell stage interphase. The middle and bottom rows show a top and side view, respectively, of the membrane (magenta) and the segmented ER (grey). Ant. is anterior, Veg. is vegetal, Ani. is animal, Post. is posterior, and NEBD is nuclear envelope breakdown. Time is in minutes:seconds. Scale bar, 30 µm.

870 **(B)** Plot of the sphericity of the cell (magenta; *N* = 14 embryos) and the ER (grey; *N* = 12 embryos) as a
871 function of time after centrosome separation (2 min, dashed vertical line) in control embryos. The
872 dashed line at 17 min indicates the time of NEBD. Error bars, standard error of the mean (s.e.m.).
873 **(C)** Plot of the angle between the long axis of the ER and the cell (blue), the long axis of the ER and the
874 CCs and spindle (green) and the long axis of the cell and the CCs and spindle (red) as a function of time
875 after centrosome separation (2 min, dashed vertical line) in control embryos. The dashed line at 17
876 min indicates the time of NEBD. Error bars, standard deviation (s.d.). Mean and s.d. were estimated by
877 bootstrap method (5000 iterations).
878 **(D)** 3D plots of the average long axis of the cell (magenta), the long axis of the ER (grey), and the CCs
879 and spindle (green) at 2, 12, 17, and 24 minutes of the left cells of ascidian embryos after metaphase
880 of the 1-cell stage. NEBD is nuclear envelope breakdown. For visualization purposes, the length of the
881 long axis of the cell (magenta) and the CCs (green) are doubled.
882 **(E)** Brightfield, confocal fluorescent images of a central z-slide of the plasma membrane (magenta),
883 and maximum intensity projections of centrosomes (green) in a representative ascidian embryo in Ca^{2+}
884 and Mg^{2+}-free sea water (CMF) from 1-cell stage metaphase to 4-cell stage interphase. Ant. is anterior,
885 Veg. is vegetal, Ani. is animal, Post. is posterior, and NEBD is nuclear envelope breakdown. Time is in
886 minutes:seconds. Scale bar, 40 µm.
887 **(E')** Plot of the rotation and tilt angles between the CCs and the spindle at 2-cell stage and the spindle
888 at 1-cell stage as a function of time after centrosome separation (2 min, dashed vertical line) in control
889 embryos (*N* = 9 embryos, *n* = 18 cells) and embryos in CMF (*N* = 10 embryos, *n* = 20 cells). The dashed
890 line at 17 min indicates the time of NEBD. Error bars, standard error of the mean (s.e.m.).
891 **(E'')** Plot of the initial (Centrosome separation) and final (Metaphase 2-cell) rotation (left) and tilt
892 (right) angles between the CCs and the spindle at 2-cell stage and the spindle at 1-cell stage in control
893 embryos (*N* = 9 embryos, *n* = 18 cells; rotation: paired Wilcoxon test, *P=0.0131; tilt: paired Wilcoxon
894 test, *P=0.0250) and embryos in CMF (*N* = 10 embryos, *n* = 20 cells; rotation and tilt: paired t test, ns -
895 not significant). Control vs. CMF rotation angle: Kruskal-Wallis test (*P=0.0194) with Dunn's multiple
896 comparisons test (ns – not significant, *P=0.0276). Control vs. CMF tilt angle: Kruskal-Wallis test (ns –
897 not significant) with Dunn's multiple comparisons test (ns – not significant).
898 **(F)** Confocal fluorescent images of the endoplasmic reticulum (top row) and its segmentation (middle
899 row is the top view and bottom row is the side view) in a representative ascidian embryo from 1-cell
900 stage metaphase to 4-cell stage interphase in CMF. Ant. is anterior, Veg. is vegetal, Ani. is animal, Post.
901 is posterior, and NEBD is nuclear envelope breakdown. Time is in minutes:seconds. Scale bar, 30 µm.
902 **(G)** Plot of the sphericity of the cell (magenta; *N* = 4 embryos) and the ER (grey; *N* = 10 embryos) as a
903 function of time after centrosome separation (2 min, dashed vertical line) in embryos incubated in CMF
904 sea water. The dashed line at 17 min indicates the time of NEBD. Error bars, standard error of the mean
905 (s.e.m.).
906 **(H)** Plot of the angle between the long axis of the ER and the CCs and spindle as a function of time after
907 centrosome separation (2 min, dashed vertical line) in control embryos (green, taken from C) and in
908 CMF-cultured embryos (orange). The dashed line at 17 min indicates the time of NEBD. Error bars,
909 standard deviation (s.d.).
910
911
912
913
914

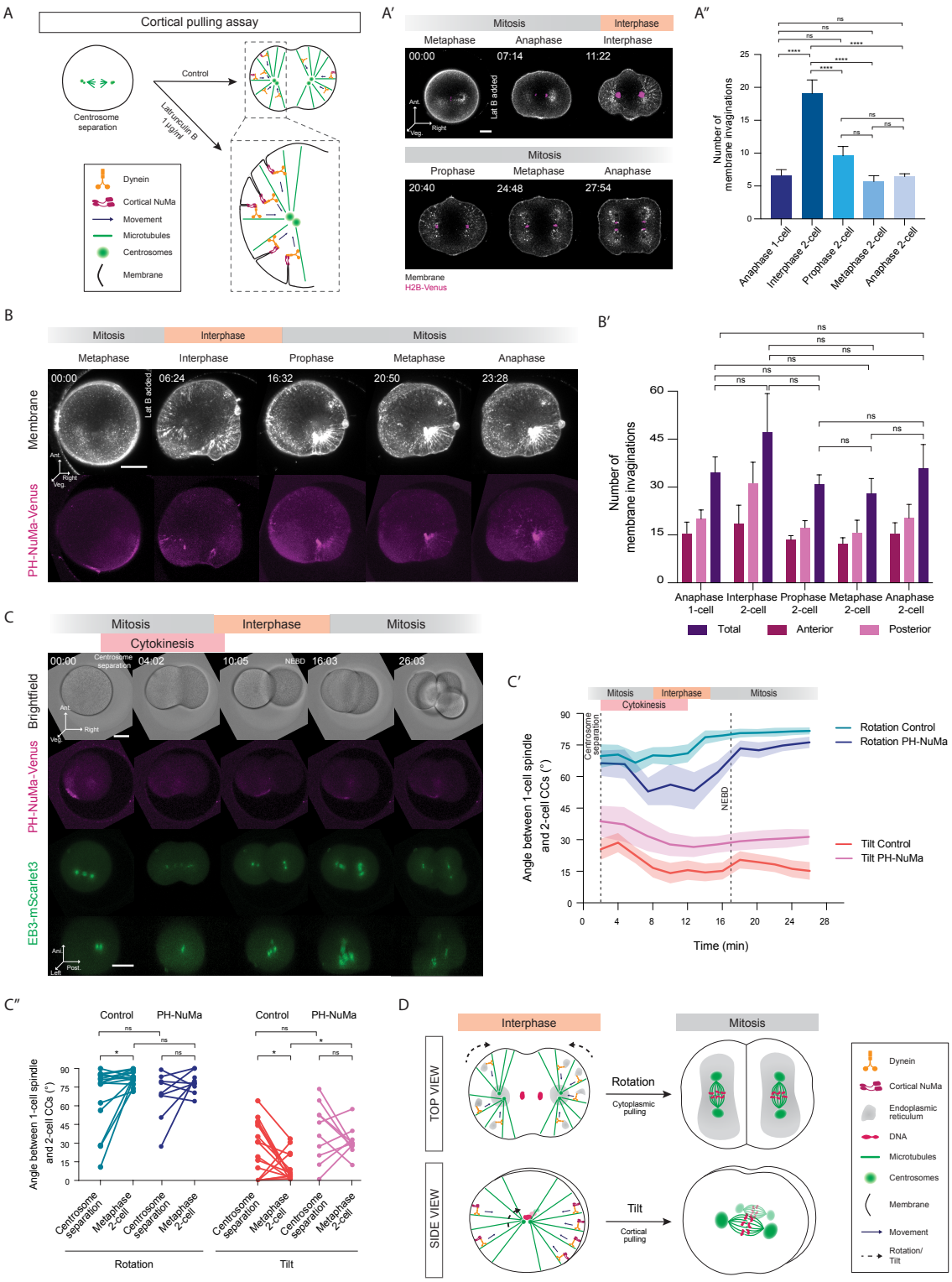

Figure 5: The tilt along the anterior-posterior axis is controlled by cortical pulling forces.

(A) Schematic representation of the cortical pulling assay to test the presence of cortical pulling sites by the formation of membrane invaginations towards the CCs in a soft-cortex ascidian embryo.

(A') Confocal maximum intensity projections over 6 central z-slices of the plasma membrane (grey) and DNA (magenta) in a representative ascidian embryo from 1-cell stage metaphase to 2-cell stage

anaphase, treated with 1µg/ml Latrunculin B from 1-cell stage anaphase. Ant. is anterior, Veg. is vegetal. Time is in minutes:seconds. Scale bar, 30 µm.

(A'') Bar plot of the average number of membrane invaginations as a function of the cell cycle stage. (*N* = 13 embryos). One-way ANOVA (****P<0.0001) and Tukey's multiple comparisons tests (****P<0.0001; ns - not significant). Error bars, standard error of the mean (s.e.m.).

(B) Confocal maximum intensity projections over 6 central z-slices of PH-NuMA (magenta) and membrane (grey) in ascidian embryos expressing PH-NuMA and treated with 1µg/ml Latrunculin B from 1-cell stage anaphase. Scale bar, 40µm.

(B') Bar plot of the average number of membrane invaginations (anterior, posterior, and total) as a function of the cell cycle stage in embryos expressing PH-NuMA and treated with 1µg/ml Latrunculin B. (*N* = 4 embryos). Kruskal-Wallis test (ns – not significant) and Dunn's multiple comparisons tests (ns - not significant). Error bars, standard error of the mean (s.e.m.).

(C) Brightfield and maximum intensity projections of confocal fluorescent images of PH-NuMA (magenta) and centrosomes (green) in embryos expressing PH-NuMA. Ant. is anterior, Veg. is vegetal, Ani. is animal, Post. Is posterior. Time is in minutes:seconds. Scale bar, 40 µm.

(C') Plot of the rotation and tilt angles between the CCs and the spindle at 2-cell stage and the spindle at 1-cell stage as a function of time after centrosome separation (2 min, dashed vertical line) in control embryos (*N* = 9 embryos, *n* = 18 cells) and embryos expressing PH-NuMA (*N* = 5 embryos, *n* = 10 cells). The dashed line at 17 min indicates the time of NEBD. Error bars, standard error of the mean (s.e.m.).

(C'') Plot of the initial (Centrosome separation) and final (Metaphase 2-cell) rotation (left) and tilt (right) angles between the CCs and the spindle at 2-cell stage and the spindle at 1-cell stage in control embryos (*N* = 9 embryos, *n* = 18 cells; rotation: paired Wilcoxon test, *P=0.0131; tilt: paired Wilcoxon test, *P=0.0250) and embryos expressing PH-NuMA (*N* = 7 embryos, *n* = 14 cells; rotation and tilt: paired t test, ns - not significant). Control vs. PH-NuMA rotation angle: Kruskal-Wallis (*P=0.0201) with Dunn's multiple comparisons test (ns – not significant). Control vs. PH-NuMA tilt angle: Kruskal-Wallis (**P=0.0073) with Dunn's multiple comparisons test (ns – not significant, *P=0.0169).

(D) Schematic model of the two mechanisms controlling the positioning of the CCs during the 2-cell stage: cytoplasmic dynein-dependent pulling along astral microtubules controls the 90°C rotation of the CCs with respect to the 1-cell stage mitotic spindle. Dynein motors on the surface of the ER are pulled towards the CCs, thus forming the pericentromeric ER domains. These domains, in turn, act as a proxy for cell shape, dictating the rotation of the CCs during interphase to generate a square 4-cell stage embryo. Concomitantly with cytoplasmic pulling, cortical dynein generates cortical pulling forces at the end of astral microtubules that control the tilt of the CCs, ensuring the coplanarity of sister CCs and the planar geometry of the 4-cell stage ascidian embryo.

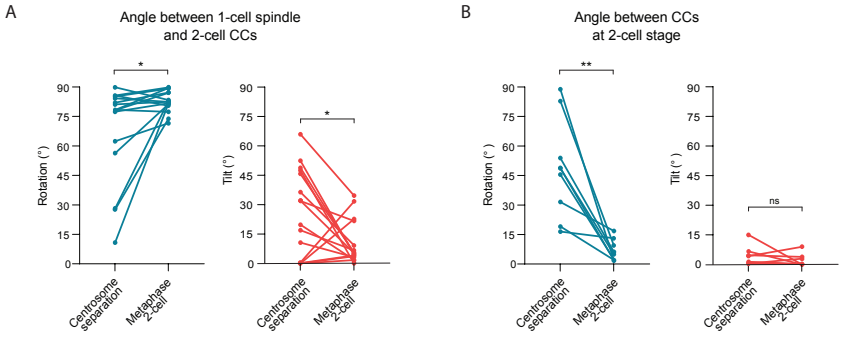

Figure S1: CCs of sister cells become parallel and coplanar at the 2-cell stage (relative to Fig. 1).
(A) Plot of the initial (Centrosome separation) and final (Metaphase 2-cell) rotation (left) and tilt (right) angles between the CCs and the spindle at 2-cell stage and the spindle at 1-cell stage (*N* = 9 embryos, *n* = 18 cells; rotation: paired Wilcoxon test, *P=0.0131; tilt: paired Wilcoxon test, *P=0.0250).
(B) Plot of the initial (Centrosome separation) and final (Metaphase 2-cell) rotation (left) and tilt (right) angles between he left and right CCs and spindles at 2-cell stage (*N* = 9 embryos; rotation: paired t test, **P=0.0017; tilt: paired Wilcoxon test, ns – not significant).

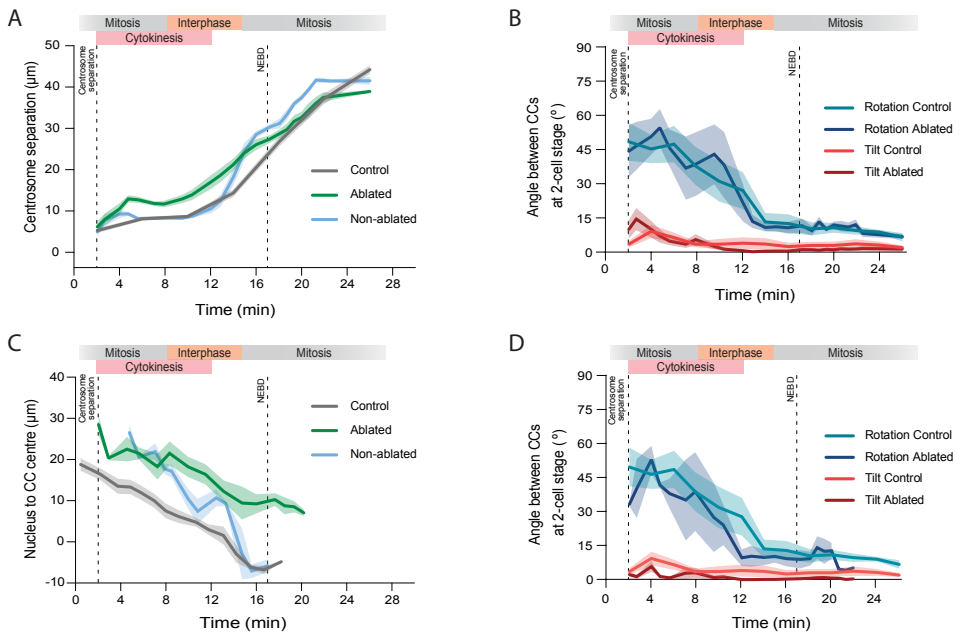

Figure S2: Centrosome migration and alignment in laser-ablated embryos (relative to Fig. 2).
(A) Plot of the separation of centrosomes within a CC as a function of time after centrosome separation (2 min, dashed vertical line) in control embryos (grey; *N* = 9 embryos, *n* = 18 cells), ablated cell (green; *N* = 5 embryos, *n* = 5 cells), and non-ablated cell (blue; *N* = 5 embryos, *n* = 5 cells) in laser-ablated embryos between the centrosomes. The dashed line at 17 min indicates the time of NEBD. Error bars, standard error of the mean (s.e.m.).
(B) Plot of the rotation and tilt angles between the CCs and the spindle of the left and right cells at 2-cell stage as a function of time after centrosome separation (2 min, dashed vertical line) in control (*N* = 9 embryos) and ablated embryos between the centrosomes in one cell (*N* = 5 embryos. The dashed line at 17 min indicates the time of NEBD. Error bars, standard error of the mean (s.e.m.).
(C) Plot of the distance between the edge of the nucleus and the centre of the CC as a function of time after centrosome separation (2 min, dashed vertical line) in control embryos (grey; *N* = 6 embryos, *n* = 12 cells), ablated cell (green; *N* = 4 embryos, *n* = 4 cells), and non-ablated cell (blue; *N* = 4 embryos, *n* = 4 cells) in laser-ablated embryos between the centrosomes and the nucleus. The dashed line at 17 min indicates the time of NEBD. Error bars, standard error of the mean (s.e.m.).
(D) Plot of the rotation and tilt angles between the CCs and the spindle of the left and right cells at 2-cell stage as a function of time after centrosome separation (2 min, dashed vertical line) in control (*N* = 9 embryos) and ablated embryos between the centrosomes and the nucleus in one cell (*N* = 4 embryos). The dashed line at 17 min indicates the time of NEBD. Error bars, standard error of the mean (s.e.m.).

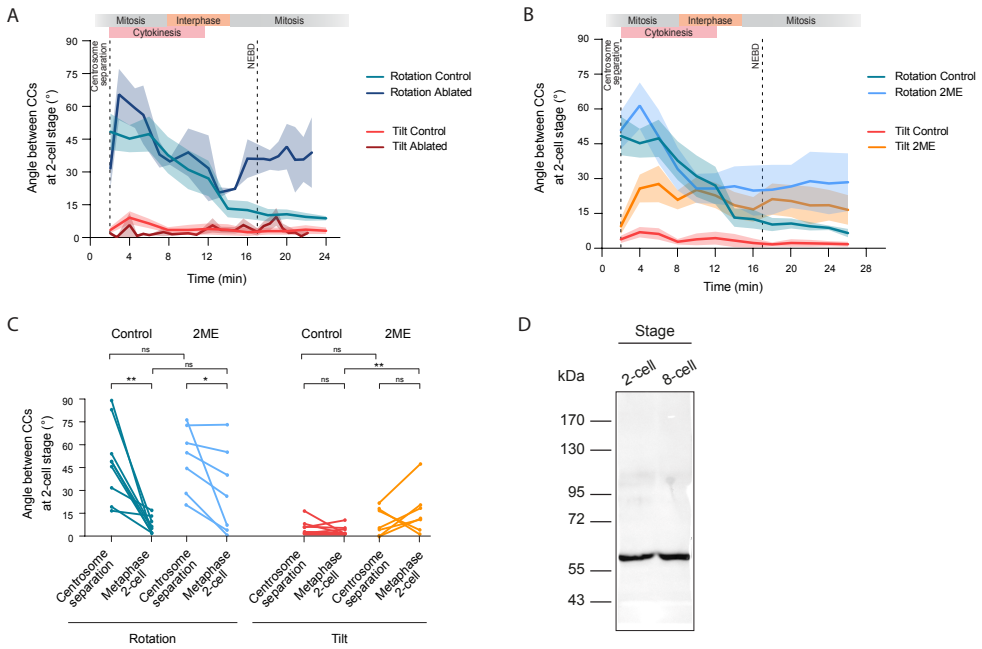

Figure S3: Centrosome alignment relies on forces generated along astral microtubules (relative to Fig. 3).

(A) Plot of the rotation and tilt angles between the CCs and the spindle of the left and right cells at 2-cell stage as a function of time after centrosome separation (2 min, dashed vertical line) in control embryos (*N* = 9 embryos), ablated cell (*N* = 4 embryos, *n* = 4 cells), and non-ablated cell (*N* = 4 embryos, *n* = 4 cells) in laser-ablated embryos. The dashed line at 17 min indicates the time of NEBD. Error bars, standard error of the mean (s.e.m.).

(B) Plot of the rotation and tilt angles between the CCs and the spindle of the left and right cells at 2-cell stage as a function of time after centrosome separation (2 min, dashed vertical line) in control (*N* = 9 embryos) and 2-methoxyestradiol-treated (*N* = 7 embryos). The dashed line at 17 min indicates the time of NEBD. Error bars, standard error of the mean (s.e.m.).

(C) Plot of the initial (Centrosome separation) and final (Metaphase 2-cell) rotation (left) and tilt (right) angles between the left and right CCs and spindle at 2-cell stage in control embryos (*N* = 9 embryos; rotation: paired Wilcoxon test, *P=0.0131; tilt: paired Wilcoxon test, *P=0.0250) and embryos treated with 2ME (*N* = 7 embryos; rotation: paired t test (*P=0.0462); tilt: paired t test (ns – not significant)). Control vs. 2ME rotation angle: one-way ANOVA (***P=0.0005) with Šídák's multiple comparisons test (ns – not significant). Control vs. 2ME tilt angle: Kruskal-Wallis test (*P=0.0186) with Dunn's multiple comparisons test (ns – not significant, **P=0.0040).

(D) Western blot image of the specificity of the ascidian anti-dynactin antibody in ascidian 2-cell and 8-cell stage embryos.

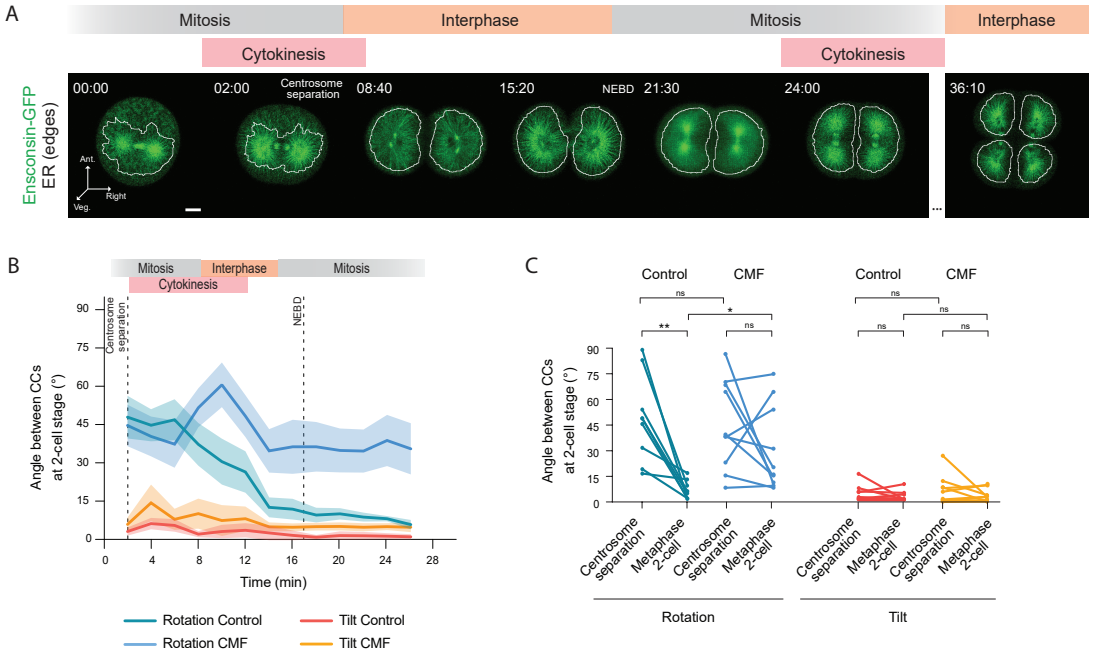

Figure S4: Cytoplasmic pulling controls rotation angles (relative to Fig. 4).

(A) Maximum intensity projections of confocal fluorescent images of microtubules (green) and the edges of the ER cloud around spindles (white) in a representative ascidian embryo from 1-cell stage metaphase to 4-cell stage interphase. Ant. is anterior, Veg. is vegetal, and NEBD is nuclear envelope breakdown. Time is in minutes:seconds. Scale bar, 30 µm.

(B) Plot of the rotation and tilt angles between the CCs and the spindle of the left and right cells at 2-cell stage as a function of time after centrosome separation (2 min, dashed vertical line) in control (*N* = 9 embryos) and embryos in CMF (*N* = 10 embryos). The dashed line at 17 min indicates the time of NEBD. Error bars, standard error of the mean (s.e.m.).

(C) Plot of the initial (Centrosome separation) and final (Metaphase 2-cell) rotation (left) and tilt (right) angles between the left and right CCs and spindle at 2-cell stage in control embryos (*N* = 9 embryos; rotation: paired Wilcoxon test, *P=0.0131; tilt: paired Wilcoxon test, *P=0.0250) and embryos in CMF (*N* = 10 embryos; rotation: paired t test, ns - not significant; tilt: paired t test, ns – not significant). Control vs. CMF rotation angle: one-way ANOVA (***P=0.0010) with Šídák's multiple comparisons test (ns – not significant, *P=0.0431). Control vs. CMF tilt angle: Kruskal-Wallis (ns – not significant) with Dunn's multiple comparisons test ns – not significant).

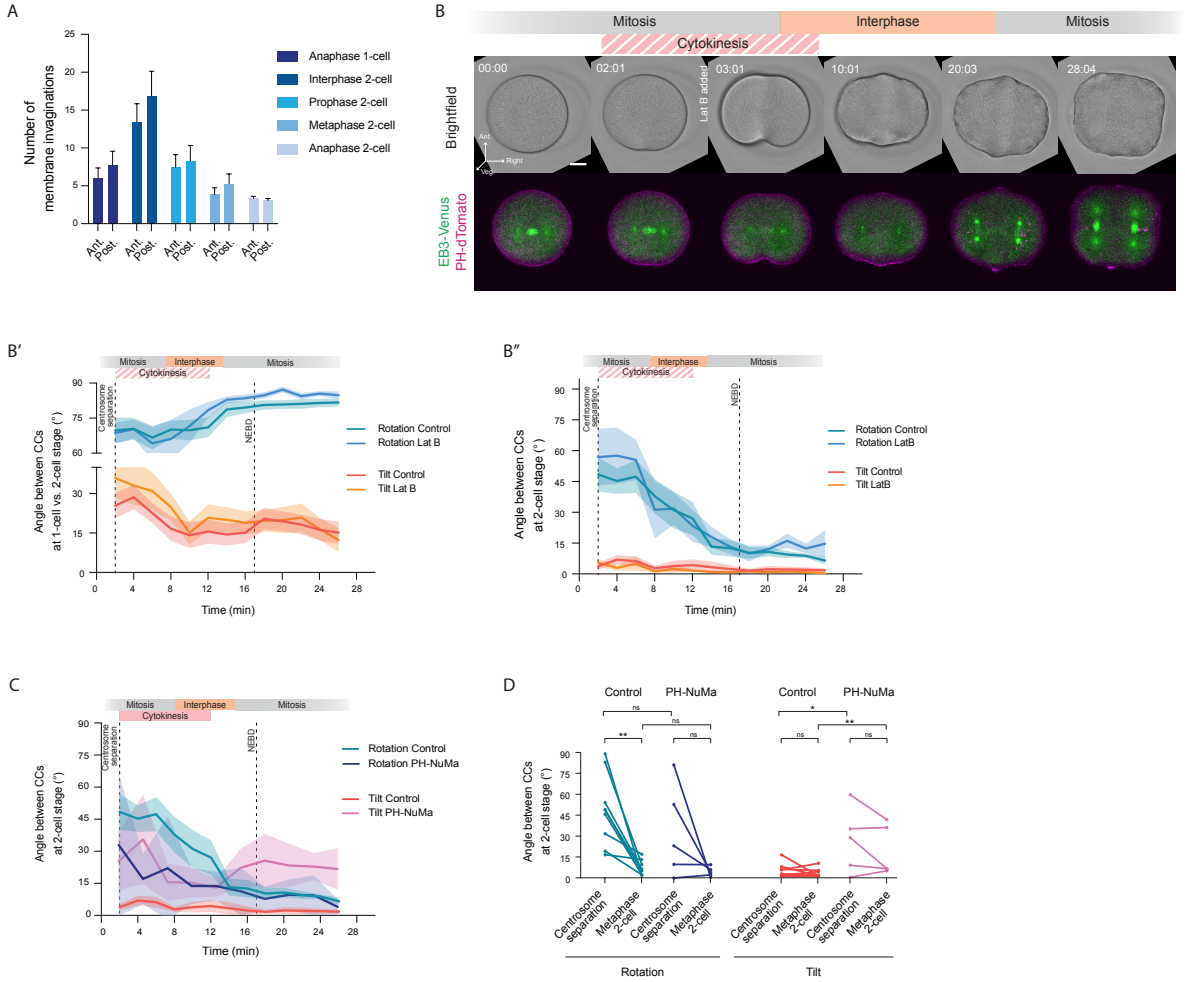

Figure S5: Cortical pulling is increased in the posterior of the ascidian 2-cell stage embryo (relative to Fig. 5).

(A) Bar plot of the average number of membrane invaginations at the anterior (Ant.) and posterior (Post.) sides of the embryo as a function of the cell cycle stage. Data is taken from Fig. 5A''.

(B) Brightfield and confocal fluorescent images of a central z-slice of the plasma membrane (magenta), and maximum intensity projections of centrosomes (green) in a representative ascidian embryo from 1-cell stage metaphase to 2-cell stage metaphase treated with 1 µg/ml Latrunculin B at 1-cell stage anaphase. Ant. is anterior, Veg. is vegetal. Time is in minutes:seconds. Scale bar, 30 µm.

(B') Plot of the rotation and tilt angles between the CCs and the spindle at 2-cell stage and the spindle at 1-cell stage as a function of time after centrosome separation (2 min, dashed vertical line) in control embryos (*N* = 9 embryos, *n* = 18 cells) and Latrunculin B-treated embryos (*N* = 5 embryos, *n* = 10 cells). The dashed line at 17 min indicates the time of NEBD. Error bars, standard error of the mean (s.e.m.).

(B'') Plot of the rotation and tilt angles between the CCs and the spindle of the left and right cells at 2-cell stage as a function of time after centrosome separation (2 min, dashed vertical line) in control (*N* = 9 embryos) and Latrunculin B-treated (*N* = 5 embryos). The dashed line at 17 min indicates the time of NEBD. Error bars, standard error of the mean (s.e.m.).

(C) Plot of the rotation and tilt angles between the CCs and the spindle of the left and right cells at 2-cell stage as a function of time after centrosome separation (2 min, dashed vertical line) in control (*N* = 9 embryos) and embryos expressing PH-NuMA (*N* = 5 embryos, *n* = 10 cells). The dashed line at 17 min indicates the time of NEBD. Error bars, standard error of the mean (s.e.m.).

(D) Plot of the initial (Centrosome separation) and final (Metaphase 2-cell) rotation (left) and tilt (right) angles between the left and right CCs and spindle at 2-cell stage in control embryos (*N* = 9 embryos; rotation: paired Wilcoxon test, *P=0.0131; tilt: paired Wilcoxon test, *P=0.0250) and embryos overexpressing PH-NuMA (*N* = 5 embryos; rotation: paired t test, ns - not significant; tilt: Wilcoxon test, ns – not significant). Control vs. PH-NuMA rotation angle: one-way ANOVA (***P=0.0005) with Šídák's multiple comparisons test (ns – not significant). Control vs. PH-NuMA tilt angle: Kruskal-Wallis test (*P=0.0210) with Dunn's multiple comparisons test (*P=0.0146, ns – not significant).

1140 **MOVIE LEGENDS**

1141 **Movie 1.** Centrosomal complex orientation during the first two cleavages in ascidian embryos, related
1142 to Fig. 1 and S1. Time-lapse brightfield (left panel) and fluorescent confocal video of a representative
1143 ascidian embryo injected with PH-dTomato mRNA (magenta, right panel) and EB3-3xVenus mRNA
1144 (green, right panel) to mark membrane and centrosomes, respectively. Time interval, 2 min.
1145

1146 **Movie 2.** Centrosome and nucleus migration during interphase of the 2-cell stage in ascidian embryos,
1147 related to Fig. 2. Time-lapse fluorescent confocal video of a representative ascidian embryo injected
1148 with EB3-mScarlet mRNA (green), H2B-Venus mRNA (magenta) to mark centrosomes and the DNA,
1149 respectively, and incubated in MitoTracker Deep Red (cyan) to label the mitochondria. Time interval,
1150 16 s.
1151

1152 **Movie 3.** Laser ablation of intercentrosomal microtubules during CC migration at the 2-cell stage of
1153 ascidian embryos, related to Fig. 2 and S2. Time-lapse fluorescent confocal video of a representative
1154 ascidian embryo injected with EB3-mScarlet mRNA (magenta) and Ensconsin-3xGFP mRNA (green) lo
1155 mark centrosomes and microtubules, respectively. Ablation site is indicated by the dashed line. Time
1156 interval, 12.8 s.
1157

1158 **Movie 4.** Laser ablation of microtubules between the CC and the nucleus during CC migration at the 2-
1159 cell stage of ascidian embryos, related to Fig. 2 and S2. Time-lapse fluorescent confocal video of a
1160 representative ascidian embryo injected with H2B-Venus mRNA (magenta) and Ensconsin-dTomato
1161 mRNA (green) lo mark DNA and microtubules, respectively. Ablation site is indicated by the dashed
1162 line. Time interval, 12.8 s.
1163

1164 **Movie 5.** Laser ablation of astral microtubules during CC migration at the 2-cell stage of ascidian
1165 embryos, related to Fig. 3 and S3. Time-lapse fluorescent confocal video of a representative ascidian
1166 embryo injected with EB3-mScarlet mRNA (magenta) and Ensconsin-3xGFP mRNA (green) lo mark
1167 centrosomes and microtubules, respectively. Ablation site is indicated by the dashed line. Time
1168 interval, 12.8 s.
1169

1170 **Movie 6.** Endoplasmic reticulum rearrangement during the first two cleavages in ascidian embryos,
1171 related to Fig. 4 and S4. Time-lapse fluorescent confocal video of a representative ascidian embryo
1172 injected with PH-dTomato mRNA (magenta) and Reticulon-Venus mRNA (grey) to mark the membrane
1173 and endoplasmic reticulum, respectively. Time interval, 110 s.
1174

1175 **Movie 7.** Centrosomal complex orientation during the first two cleavages in ascidian embryos cultured
1176 in Ca^{2+} and Mg^{2+}-free seawater, related to Fig. 4 and S4. Time-lapse brightfield (left panel) and
1177 fluorescent confocal video of a representative ascidian embryo injected with PH-dTomato mRNA
1178 (magenta, right panel) and EB3-3xVenus mRNA (green, right panel) to mark membrane and
1179 centrosomes, respectively. Time interval, 2 min.
1180

1181 **Movie 8.** Cortical pulling assay in control ascidian embryos, related to Fig. 5 and S5. Time-lapse
1182 fluorescent confocal video of a representative ascidian embryo treated with in 1μg/ml Latrunculin B
1183 and injected with H2B-Venus mRNA (magenta) to mark the DNA, and incubated in Cell Mask Orange
1184 to label the plasma membrane (grey). Time interval, 20 s.

1185 **Movie 9.** Cortical pulling assay in ascidian embryos expressing PH-NuMA, related to Fig. 5 and S5. Time-
1186 lapse fluorescent confocal video of a representative ascidian embryo treated with in 1μg/ml
1187 Latrunculin B and incubated in Cell Mask Orange to label the plasma membrane (grey, left panel) and
1188 injected with PH-NuMA-Venus mRNA (magenta, right panel) to mark exogenous cortical NuMA. Time
1189 interval, 16 s.
1190
1191 **Movie 10.** Centrosomal complex orientation during the first two cleavages in ascidian embryos
1192 expressing PH-NuMA to increase cortical pulling, related to Fig. 5 and S5. Time-lapse brightfield (left
1193 panel) and fluorescent confocal video of a representative ascidian embryo injected with PH-NuMA-
1194 Venus mRNA (magenta, right panel) and EB3-mScarlet3 (green, right panel) to mark exogenous cortical
1195 NuMA and centrosomes, respectively. Time interval, 2 min.
1196